Hannes-Jörg Schmiedmayer

TECHNISCHE UNIVERSITÄT WIEN
Vienna University of Technology

DIPLOMARBEIT

Arbitrary One-Dimensional Optical Dipole Potentials on an Atom Chip

ausgeführt am Atominstitut
der Technischen Universität Wien

unter der Anleitung von
Univ.Prof. Dipl.-Ing. Dr.techn. Hannes-Jörg Schmiedmayer
und
Projektass. Dipl.-Ing. Bernhard Rauer

durch

Mohammadamin Tajik

Hetzendorfer Straße 75/ 17
1120 Wien

Wien, am 17.05.2017

Mohammadamin Tajik

Acknowledgements

First and foremost, I am very grateful to Professor Schmiedmayer, not only for the exciting project, but also for giving me the opportunity to earn new experiences in an international group, in which physicists from more than fifteen nations worldwide are working together in the frontier of experimental quantum physics.

I would then like to thank Kaspar Sakmann, a patient teacher from whom I learned a lot. The door to his office was always open whenever I ran into a trouble spot or had a question.

I would like to express my sincere gratitude to my advisor Bernhard Rauer for the continuous support, for his patience, motivation, and immense knowledge in both theory and experiment. His guidance helped me in all the time of research and writing of this thesis.

Besides my advisors, I would like to thank the KRb team, Thomas Schweigler, Federica Cataldini and Sicong Ji, for discussions and proofreading.

My sincere thanks also goes to Ru-Gway Wu, Michael Trupke and Thorsten Schumm for fruitful discussions and their useful suggestions.

I would like then to thank Florian Steiner, Anne Maître for allocating a part of their lab for our setup.

I also want to thank the whole Atomchip group for all beautiful and fun moments they created, including breakfast meetings and exciting coffecorner-discussions.

My special thanks goes to Herbert Hartmann and his team in the mechanical workshop of Atominstitut for rapid handling of machining the parts needed for the setup and for supportive discussions and suggestions. I also appreciate fruitful discussions with Andrzej Pelczar and his team in the electronics workshop.

I have to acknowledge my friends Korbinian Eckstein, Angelika Monetti, Elisabeth Salomon and Christian Ramsl for everything I learned from them and for all unforgettable moments that we had during my master studies in Vienna.

Finally, I must express my very profound gratitude to my dear parents, my supportive mother-in-law, my dear aunt and my little sister for providing me with unfailing support and continuous encouragement throughout my years of study and through the process of writing this thesis. This accomplishment would not have been possible without them.

Last but not least, my special thanks goes to my dear Kamelia, for her constant support and love during my studies and her patience through the writing process. Without her all my achievements would be worthless.

Abstract

In this work, an optical system based on a digital micromirror device (DMD) is designed and built in order to realize arbitrary static and dynamic optical dipole potentials for one-dimensional (1d) quasi-condensates of ^{87}Rb created on an atom chip. The hybrid trapping configuration realized by the superposition of this optical potential with the magnetic confinement of the atom chip combines the high flexibility of optical dipole traps with the advantages of magnetic trapping, such as effective evaporative cooling and the application of radio frequency dressed state potentials. To achieve maximal flexibility, automated pattern optimization procedures and selective Fourier space filtering for high grayscaling resolution are developed. This setup will enable the investigation of many different model systems addressing questions from quantum many-body physics to quantum thermodynamics.

Zussamenfassung

Im Rahmen dieser Arbeit wurde ein optischer Aufbau basierend auf einem Digital Micromirror Device (DMD) entwickelt und charakterisiert, um statische und dynamische optische Dipol-Potenziale für eindimensionale (1d) Quasi-Kondensate auf einem Atomchip zu realisieren. Die Kombination optischer Dipol-Potenziale mit magnetischen Potenzialen verbindet die höhe Flexibilität von optischen Fallen mit den Vorteilen von Magnetfallen wie z.B. effektives evaporatives Kühlen und die Anwendbarkeit von "radio frequency dressed state" Potenzialen. Um die maximale Flexibilität der Potenziale zu erreichen, wurde eine automatisierte Muster-Optimierung für den DMD entwickelt und hohe Graustufen-Auflösung durch Anwendung eines Fourier-Raum-Filters erreicht. Das aufgebaute System ermöglicht das Erforschen neuer Aspekte der Dynamik von 1d Quantensystemen in Bereichen der Quantenvielteilchenphysik bis hin zu Quantenthermodynamik.

Contents

Chapter 1

Introduction

In 1925, Albert Einstein published the second part of a paper, in which he developed a quantum theory for monatomic ideal gases [1, 2]. His theory was based on a derivation of Planck's radiation formula, suggested by Satyendra Nath Bose earlier in 1924 [3]. The famous concept of Bose-Einstein statistics for non-interacting indistinguishable particles originates from the work of the two gentlemen. Further discussing this theory, Einstein showed that for a given temperature, a quantum ideal gas can be compressed only up to a certain density. He claimed that further compressing will cause a part of the gas to condensate and to populate the ground state of the system. This was the first theoretical consideration of a phenomenon which is called Bose-Einstein condensation today. Meanwhile many tools and techniques developed in the field of atomic physics, with the invention of the laser being the most prominent one [4]. Laser cooling techniques, including the Doppler cooling [5] and the Zeeman slower [6], evaporative cooling [7] and magnetic trapping [8, 9] are a few other crucial experimental tools developed to make the creation of a BEC possible [10, 11]. Since 1995, the BEC has become a powerful platform, enabling physicist to explore many aspects of physics, from investigating textbook Hamiltonians in condensed matter physics [12] to simulating analogue gravity models [13].

One of the powerful tools to realize and control BECs are atom chips [14]. An atom chip is an integrated micro fabricated device, which provides a compact and robust platform to cool down, trap and manipulate both bosonic and fermionic species. However the trapping techniques on an atom chip are limited by the magnetic field configurations which can be produced by the miniaturized wires on its surface. Exploiting the interaction between light and matter is a way to overcome this obstacle [15].

In this work, an optical system is designed to realize arbitrary optical dipole potentials for a one-dimensional (1d) quasi-condensates, produced on an atom chip. In this setup, a digital micromirror device (DMD) [16] is used to perform 1d beam shaping, allowing for

an arbitrary control of the light intensity pattern at the position of the atoms. The dipole potential created in this process is superposed with the magnetic confinement of the atom chip trap all in all realizing a more versatile trapping geometry.

In this manuscript, chapter 2 introduces the basic concepts behind the trapping of neutral atoms in magnetic and optical potentials. In this context, two well-known magnetic configurations, namely quadrupole and Ioffe-Pritchard configurations are discussed in more detail. Chapter 3 gives an overview of the experimental setup in which the arbitrary dipole trap will be employed with a focus on the trapping techniques used in the experiment. A typical experimental cycle is discussed at the end of this chapter. Chapter 4 is dedicated to explain how the image of a two-dimensional binary DMD pattern can be exploited to realize a one-dimensional optical dipole trap. The optical setup which is designed and built to image the DMD pattern is described in chapter 5. In chapter 6, a probabilistic method is introduced with which arbitrary 1d potentials can be designed and optimized. The final chapter summarizes the important points of the thesis and gives an outlook at the possible future applications of the setup.

Chapter 2

Trapping Neutral Atoms

Investigating the interesting physics related to ultra-cold quantum gases requires the atoms to be thermally disconnected from its "hot" environment, hence for all these types of experiments, ultra high vacuum is required. To reach the quantum regime, the atoms have to be cooled down with different techniques, a few of which were mentioned in chapter 1. During this cooling process, the gas needs to be confined in space, namely a trap so that further cooling and manipulation be possible.

Today, a variety of trapping techniques can be used, depending on the experimental requirements. Magnetic potentials [9], electrostatic potentials [17], radio frequency (rf) dressed state potentials [18] as well as optical dipole potentials [15] are among the trapping potentials which have been demonstrated experimentally so far.

In this chapter, magnetic traps and optical dipole traps are introduced and discussed in more detail as they are the building blocks of the experiment presented in this manuscript.

2.1 Magnetic Potentials for Neutral Atoms

The force acting on a particle with a magnetic dipole moment $\boldsymbol{\mu}$ in a magnetic field $\boldsymbol{B}$ is given by $\boldsymbol{\nabla}(-\boldsymbol{\mu}\cdot\boldsymbol{B})$. The magnetic dipole moment for a particle with angular momentum $\boldsymbol{F}$, is $\boldsymbol{\mu} = -g_{\mathrm{F}}\mu_{\mathrm{B}}\boldsymbol{F}$ with g_{F} being the Landé g-factor corresponding to $\boldsymbol{F}$ and μ_{B} the Bohr magneton. For a weak magnetic field, the Zeeman energy levels are given by

$$U_{\mathrm{mag}}(\boldsymbol{r}) = -\boldsymbol{\mu}\cdot\boldsymbol{B}(\boldsymbol{r}) = m_{\mathrm{F}}g_{\mathrm{F}}\mu_{\mathrm{B}}B(\boldsymbol{r})\ , \tag{2.1}$$

in which m_{F} is the quantum number of the z-component of $\boldsymbol{F}$ and $B(\boldsymbol{r}) = |\boldsymbol{B}(\boldsymbol{r})|$, the magnitude of the field. Note that to evaluate the dot product in equation 2.1, it is assumed that the

quantization axis of the atom (z-axis in this case) coincides with the direction of the magnetic field.

If an atom is in a state for which $m_F g_F > 0$, the atom moves toward the spatial regions with lower magnetic field, in order to minimize its energy. These states are called low-field seeking states. Otherwise, if $m_F g_F < 0$, the atom is drawn to regions with stronger magnetic fields. These states are called high-field seeking states. High-field seeking states can not be confined in a specific region of the free space, because according to the Maxwell's equations, it is forbidden to have a magnetic field maximum in free space.

Consider a frame of reference which is fixed to an atom in a low-field seeking state that is moving in a trap with a minimum in magnetic field. In this frame of reference, the position of the atom is fixed and the magnetic field acting on the atom is a time varying field $\boldsymbol{B}(t)$. As long as the quantization axis of the atom can adiabatically follow the changes of the direction of the magnetic field, the atom will be trapped and equation 2.1 will hold. Otherwise a spin flip can occur which leaves the atom in an untrapped state. Therefore, the trap is stable if the direction of the magnetic field $\theta(t)$ as seen by atom, changes slower than the Larmor frequency $\omega_L(t) = m_F g_F \mu_B B(t)/\hbar$,

$$\frac{d\theta(t)}{dt} < \omega_L(t) \; . \tag{2.2}$$

This condition can easily be violated in regions near the minima where the magnetic field is very small causing spin flips due to the so called Majorana transitions. This will be the case for traps where the magnetic field has a zero crossing or traps which have a very small finite minima.

In the following some basic but important trapping configurations are introduced.

2.1.1 Quadrupole Traps

Quadrupole traps are configurations in which the minimum of the magnetic trap is a zero crossing of the magnetic field. The simplest quadrupole field configuration can be written as $\boldsymbol{B}(\boldsymbol{r}) = B'_x x\hat{\boldsymbol{x}} + B'_y y\hat{\boldsymbol{y}} + B'_z z\hat{\boldsymbol{z}}$, in which B'_x, B'_y and B'_z are constants for which equation holds $B'_x + B'_y + B'_z = 0$, according to Maxwell's equations. The magnitude of the field $B(\boldsymbol{r}) = \sqrt{(B'_x x)^2 + (B'_y y)^2 + (B'_z z)^2}$ is linear in each spatial dimension and has a zero minimum in the center of the trap. For the central region of such traps, Majorana losses are unavoidable. However this effect is suppressed if the atoms are hot enough [19]. This is why these traps are widely used in initial cooling and trapping stages. The simplest way to realize a quadrupole trap is to use two coils in anti-Helmholtz configuration [9]. A U-shaped wire trap [20] discussed in section 2.1.3 can also used to form a quadrupole trap .

2.1.2 Ioffe-Pritchard Traps

Designing desired field configurations is not as trivial as one might think, because it is highly constrained by Maxwell equations. The following field configuration, which leads to a harmonic trap with a non-zero minimum, is known as Ioffe-Pritchard configuration [8, 21].

$$\begin{aligned}\boldsymbol{B}(\boldsymbol{r}) = B_{\text{bias}}\,\hat{\boldsymbol{x}} + \frac{B''}{2}\big(x^2 - \frac{1}{2}(y^2+z^2)\big)\,\hat{\boldsymbol{x}} \\ + (-B'\,y - \frac{B''}{2}\,xy)\,\hat{\boldsymbol{y}} \\ + (B'\,z - \frac{B''}{2}\,xz)\,\hat{\boldsymbol{z}}\,.\end{aligned} \tag{2.3}$$

The magnitude of this field around the origin, where $x \ll \sqrt{B_{\text{bias}}/B''}$ and $y,z \ll B_{\text{bias}}/B'$, is approximately given by

$$B(\boldsymbol{r}) = B_{\text{bias}} + \frac{B''}{2}x^2 + \frac{1}{2}\big(\frac{B'^2}{B_{\text{bias}}} - \frac{B''}{2}\big)(y^2+z^2)\,. \tag{2.4}$$

Calculating the magnetic potential using equation 2.1 and bringing it to the familiar form of harmonic trap $U_{\text{mag}}(\boldsymbol{r}) = M\omega_{\parallel}^2\,x^2/2 + M\omega_{\perp}^2\,(y^2+z^2)/2$, with M being the mass of an atom, yields the following equations for the longitudinal and transversal trap frequencies,

$$\omega_{\parallel} = \sqrt{\frac{m_{\text{F}}g_{\text{F}}\mu_{\text{B}}}{M}B''} \qquad\qquad \omega_{\perp} = \sqrt{\frac{m_{\text{F}}g_{\text{F}}\mu_{\text{B}}}{M}\big(\frac{B'^2}{B_{\text{bias}}} - \frac{B''}{2}\big)}\,. \tag{2.5}$$

The aspect ratio $AR = \omega_{\parallel}/\omega_{\perp}$ shows how isotropic the trap is. Equation 2.5 suggest that for an ideal Ioffe-Pritchard configuration, the AR can be tuned by adjusting the parameters B'' and B'^2/B_{bias}. Using this feature a wide range of magnetic traps are realised, from prolate (cigar shaped) traps ($AR \ll 1$), to isotropic ($AR \approx 1$) and on to oblate (pancake shaped) traps ($AR \gg 1$) [22].

Adjustability and having a non-zero trap minimum, makes the Ioffe-Pritchard configuration a widely used configuration for trapping ultra-cold atoms. A Z-shaped wire trap introduced in next section can be used to realize a Ioffe-Pritchard field configuration.

2.1.3 Wire Traps

The magnetic field created by an infinitely thin and infinitely long wire, carrying the current I in the $-y$-direction, shown in figure 2.1 is given by

$$\boldsymbol{B}(\boldsymbol{r}) = \frac{\mu_0 I}{2\pi}\left(-\frac{z}{x^2+z^2}\hat{\boldsymbol{x}} + \frac{x}{x^2+z^2}\hat{\boldsymbol{z}}\right), \tag{2.6}$$

in which μ_0 is the magnetic permeability of free space. The magnitude of this field, plotted in red in figure 2.1, is inversely proportional to the distance from the wire, $\sqrt{x^2+z^2}$.

Adding a constant bias field $\boldsymbol{B}_{\text{bias}}(\boldsymbol{r}) = (\mu_0 I/2\pi d)\hat{\boldsymbol{z}}$ realizes a two-dimensional (2d) quadrupole trap in the xz-plane with a zero field minimum at $x = -d$ as demonstrated in figure 2.1.

Developing this idea, a variety of wire configurations can be designed to realize 3d quadrupole or Ioffe-Pritchard traps. Two fundamental examples are U-shaped and Z-shaped wire traps, described in figure 2.2. U-shaped wire configurations are used to realize a 3d quadrupole trap, while Z-shaped wire configurations produce Ioffe-Pritchard traps. Both U-shaped and Z-shaped wire configurations are in principle an approximation to a more general configuration, namely H-shaped configuration [19]. It is important to note that the approximation of infinitely thin and long wire is not valid if the distance of atoms from the wire is comparable to the width of the wire. The magnetic field configuration of real wires can be calculated numerically using the Biot-Savart law.

2.2 Optical Dipole Potentials for Neutral Atoms

The interaction between neutral atoms and light fields, laser light for example, can be exploited trapping. In the following, a simple model [15] is used to describe this interaction and to obtain the trapping potential $U_{\text{dip}}(r)$.

Oscillator Model of Optical Dipole Potentials

An oscillating electric field with frequency ω, $\boldsymbol{E}(\boldsymbol{r},t) = \tilde{\boldsymbol{E}}(\boldsymbol{r})e^{-i\omega t} + c.c.$, polarizes neutral atoms and induces a dipole moment $\boldsymbol{p}(\boldsymbol{r},t) = \tilde{\boldsymbol{p}}(\boldsymbol{r})e^{-i\omega t} + c.c.$. The amplitude $\tilde{\boldsymbol{p}}$ of this dipole moment is related to the field amplitude by the complex polarisability α in a simple way: $\tilde{\boldsymbol{p}} = \alpha\tilde{\boldsymbol{E}}$. The polarisability can be calculated considering the atom in the Lorentz's model of a classical oscillator

$$\alpha = \frac{e^2}{m_{\text{e}}}\frac{1}{\omega_0^2 - \omega^2 - i\omega\Gamma_\omega} \tag{2.7}$$

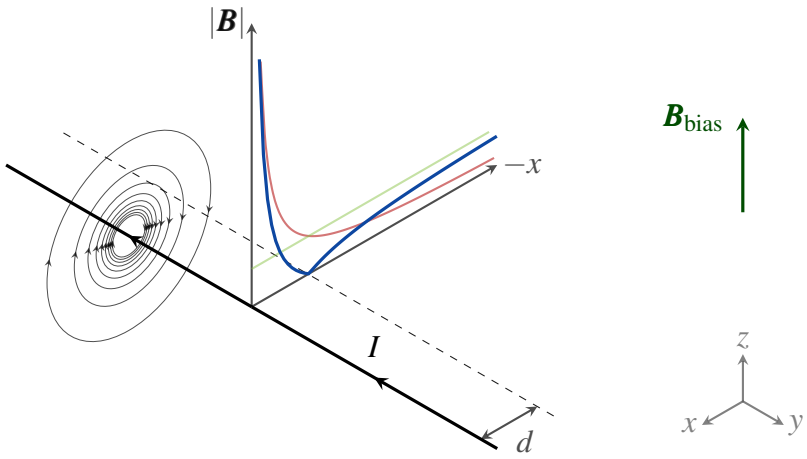

Fig. 2.1 Realization of a 2d quadrupole trap using an infinitely thin and long wire and an external bias field. The circles show the field lines of an infinitely thin and long wire carrying the current I in $-y$-direction. The red curve shows the magnitude of the field as a function of the distance from the wire. On the xy-plane this field has only a non-zero z-component. Applying an external bias field in $+z$-direction with the magnitude $B_{\text{bias}} = \mu_0 I/2\pi d$ will cancel the magnetic field of the wire at a distance d from the wire (dashed line), and produces a 2d quadrupole trap in any xz-plane. The resulting magnetic field, has the magnitude plotted in blue as a function of x on the xz-plane.

in which

$$\Gamma_\omega = \frac{e^2\omega^2}{6\pi\varepsilon_0 m_e c^3} \tag{2.8}$$

is the damping rate. Note that ω_0 is the oscillator eigenfrequency corresponding to the optical transition frequency, c is the speed of light in vacuum, ε_0 is the permittivity of free space, m_e and $-e$ are the mass and the electric charge of the electron respectively. Defining the on-resonance damping rate $\Gamma \equiv \Gamma_{\omega_0} = (\omega_0/\omega)^2\Gamma_\omega$, α can be written as

$$\alpha = 6\pi\varepsilon_0 c^3 \frac{\Gamma/\omega_0^2}{\omega_0^2 - \omega^2 - i(\omega^3/\omega_0^2)\Gamma}. \tag{2.9}$$

The interaction potential of the induced dipole moment with the electric field is given by

$$U_{\text{dip}} = -\frac{1}{2}\langle \boldsymbol{p}\boldsymbol{E}\rangle = -\frac{1}{2\varepsilon_0 c}\Re(\alpha) I(\boldsymbol{r}), \tag{2.10}$$

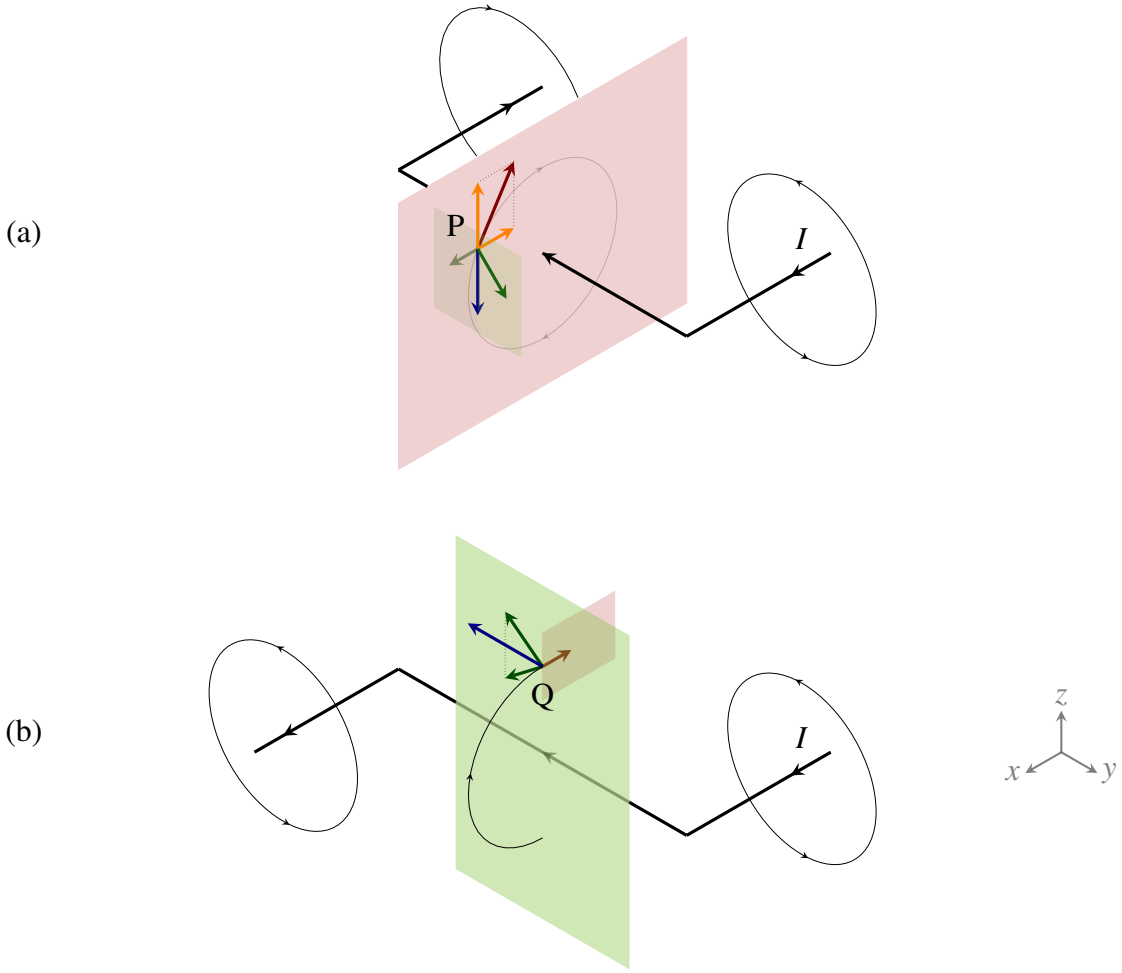

Fig. 2.2 Scheme of a U-shaped (a) and a Z-shaped (b) wire trap. In (a) the red plane is a xz-plane, placed in the middle of the wire and the green plane is a yz-plane containing the point P. At this point, the magnetic field vectors are shown for each wire segment. The two green vectors are fields created by the two side wires and the blue one is the sum of those which is merely pointing in $-z$-direction. The red vector, is the magnetic field produced by the wire segment in the middle. This red vector which lies on the red plane, can be decomposed into the two orange colored vectors. The point P is chosen such that the z-component of the red vector is equal to the blue one. This means that the total field at the point P is the orange vector pointing in the $-x$-direction. Applying a constant bias field with the same magnitude but in the opposite direction leads to a vanishing magnetic field at P and a 3d quadrupole field configuration around it. In (b) the red plane is the same as in (a) but the green plane is a centrally located yz-plane containing the middle wire segment. At the point Q, the magnetic field from the middle segment is indicated by the red vector pointing in $-x$-direction. The two green vectors show the fields created by the two side wires and the blue one is the sum of the two which is pointing only in the $-y$-direction. A bias field can be applied in $+x$-direction to cancel the red vector. This leads to a trap minimum with a finite field. It is important to note that in this scheme, all wires are considered as infinitely thin and long wires. Both wire configurations are contained in an H-shaped configuration, with parallel (b) or anti-parallel (a) currents in side wires.

in which $I(\boldsymbol{r})$ is the field intensity and $\Re(\alpha)$ the real part of the complex number α. The power absorbed by the oscillator from the driving field is given by

$$P_{\text{abs}} = \langle \dot{\boldsymbol{p}} \boldsymbol{E} \rangle = 2\omega \Im(\tilde{p}\tilde{E}^*) = \frac{\omega}{\varepsilon_0 c} \Im(\alpha) I(\boldsymbol{r}), \tag{2.11}$$

where $\Im(\alpha)$ is the imaginary part of the α. From this absorbed power, a scattering rate can be calculated, in terms of the number of photons absorbed per unit of time,

$$\Gamma_{\text{sc}} = \frac{P_{\text{abs}}}{\hbar\omega} = \frac{1}{\hbar\varepsilon_0 c} \Im(\alpha) I(\boldsymbol{r}). \tag{2.12}$$

It is important to note that the equation 2.9 is only valid in the regime of low saturation. Inserting the expression 2.9 for α into equation 2.12 and 2.10 gives

$$U_{\text{dip}}(\boldsymbol{r}) = -\frac{3\pi c^2}{2\omega_0^3} \left(\frac{\Gamma}{\omega_0 - \omega} + \frac{\Gamma}{\omega_0 + \omega} \right) I(\boldsymbol{r}) \tag{2.13}$$

$$\Gamma_{\text{sc}}(\boldsymbol{r}) = \frac{3\pi c^2}{2\hbar\omega_0^3} \left(\frac{\omega}{\omega_0} \right)^3 \left(\frac{\Gamma}{\omega_0 - \omega} + \frac{\Gamma}{\omega_0 + \omega} \right)^2 I(\boldsymbol{r}). \tag{2.14}$$

Now it is worth to take a look at the special case in which the detuning $\Delta = \omega - \omega_0$ is so small that one can set $\omega/\omega_0 \approx 1$. Using this so called rotating wave approximation equations 2.13 and 2.14 can be written in the following form:

$$U_{\text{dip}}(\boldsymbol{r}) = \frac{3\pi c^2}{2\omega_0^3} \frac{\Gamma}{\Delta} I(\boldsymbol{r}) \tag{2.15}$$

$$\Gamma_{\text{sc}}(\boldsymbol{r}) = \frac{3\pi c^2}{2\hbar\omega_0^3} \left(\frac{\Gamma}{\Delta} \right)^2 I(\boldsymbol{r}). \tag{2.16}$$

It is important to note that the interaction potential U_{dip} scales with $I(\boldsymbol{r})/\Delta$ while the scattering rate scales with $I(\boldsymbol{r})/\Delta^2$, which means, going to large detunings the scattering rate falls off faster than the potential. This allows for the realization of optical trapping potentials with negligible scattering effects.

Another interesting point understood from equation 2.15 is that for the red-detuned laser light ($\Delta < 0$) the interaction potential will be negative which means the dipole force attracts the atoms into the regions of higher laser intensity. If the laser light is blue-detuned ($\Delta > 0$) the dipole force will be repulsive and the atoms will be repelled from regions of higher intensity.

Chapter 3

Experimental Setup

In recent decades, different experimental platforms have been developed which enable physicist to study various systems of ultra-cold atoms. One of the famous and well-established platforms is the atom chip [14]. Modern technology in lithography and nano fabrication [23] is used to make miniaturised complex micro structures on a surface. These current carrying micro wires are then utilized to produce different magnetic field configurations in order to trap, cool and manipulate cold matter. Atom chip setups are compact setups in which various trapping techniques are implementable, including electrostatic potentials [17] and radio frequency (rf) dressed state potentials [18] making them highly controllable. A wide range of neutral particles can be trapped using atom chips including bosonic and fermionic nutral atoms [24], Rydberg atoms [25] and molecules [26]. Moreover, charged particles such as ions [27] and electrons [28] can also be trapped and manipulated in the chip experiments.

This chapter is dedicated to describe the setup of a chip experiment, capable of manipulating Bose-Fermi mixtures. First, an overview of the setup and its features is given. Then, the trapping techniques are discussed and finally, a typical experimental cycle is summarised.

3.1 Overview

The colloquially called KRb experiment [29–31] is designed to cool, trap and manipulate Bose-Fermi mixtures, however the setup also allows for the study of ultra-cold bosonic gases. In this manuscript only the later is considered. In the experiment samples of around ten thousand rubidium atoms (^{87}Rb) below 100 nK can be created via laser cooling and evaporative cooling techniques. The micro-fabricated gold wire chip is designed to make elongated harmonic traps with very small aspect ratios (see 2.1.2) on the order of $AR \approx 10^{-3}$. The atomic cloud in such traps can be described as a one dimensional (1d) quasi-condensate [32]. The setup consists of two vacuum chambers connected via a differential

pumping stage. First, the atoms are continuously dispensed into the so called source chamber where they are gathered in a three-beam retro-reflected magneto optical trap (MOT). At the same time, a near-resonant push beam aimed through the differential pumping stage shoots the atoms to the science chamber, where they are loaded to a mirror-MOT near the chip surface. The magnetic configurations used in each MOT will be discussed in the next section (3.2.1). In the science chamber, an intermediate trapping stage loads the atoms from the mirror-MOT to the chip trap. This stage is necessary due to the small trapping volume of the chip trap in comparison to the mirror-MOT. In the chip trap, the atoms are further cooled and can be manipulated e.g. via rf-dressed state potentials or optical dipole traps. The main measured physical quantity in the experiment is the atomic density. It is determined using time of flight (TOF) measurements, in which after turning off the traps, the cloud falls away from the chip under gravity and expands. Absorption imaging is used to determine the atomic density by recording the shadow of the expanded cloud.

3.2 Trapping Techniques

In the experiment, static magnetic traps and rf-dressed state potentials are used to cool down and manipulate the atoms. In the following, the trapping methods used in different parts of the experimental cycle are introduced.

3.2.1 Magnetic Traps

Different structures are used in the experiment to realize quadrupole and Ioffe-Pritchard trap configurations discussed in section 2.1.

- **Source chamber MOT:** Around the source chamber, three pairs of coils in anti-Helmholtz configuration are used to make a 3d quadrupole trap. As already mentioned in section 2.1.1, because of the high temperatures in this stage, Majorana losses are negligible.

- **Science chamber MOT:** The macroscopic U-structure shown in figure 3.1 along with a pair of coils in Helmholtz configuration is used to realize a quadrupole trap near the chip.

- **Chip loading traps:** A macroscopic Z-wire and h-wire (used as a smaller Z-wire) along with an external bias field are used to make an intermediate trap to load the atoms in the chip trap and also to perform a pre-cooling process.

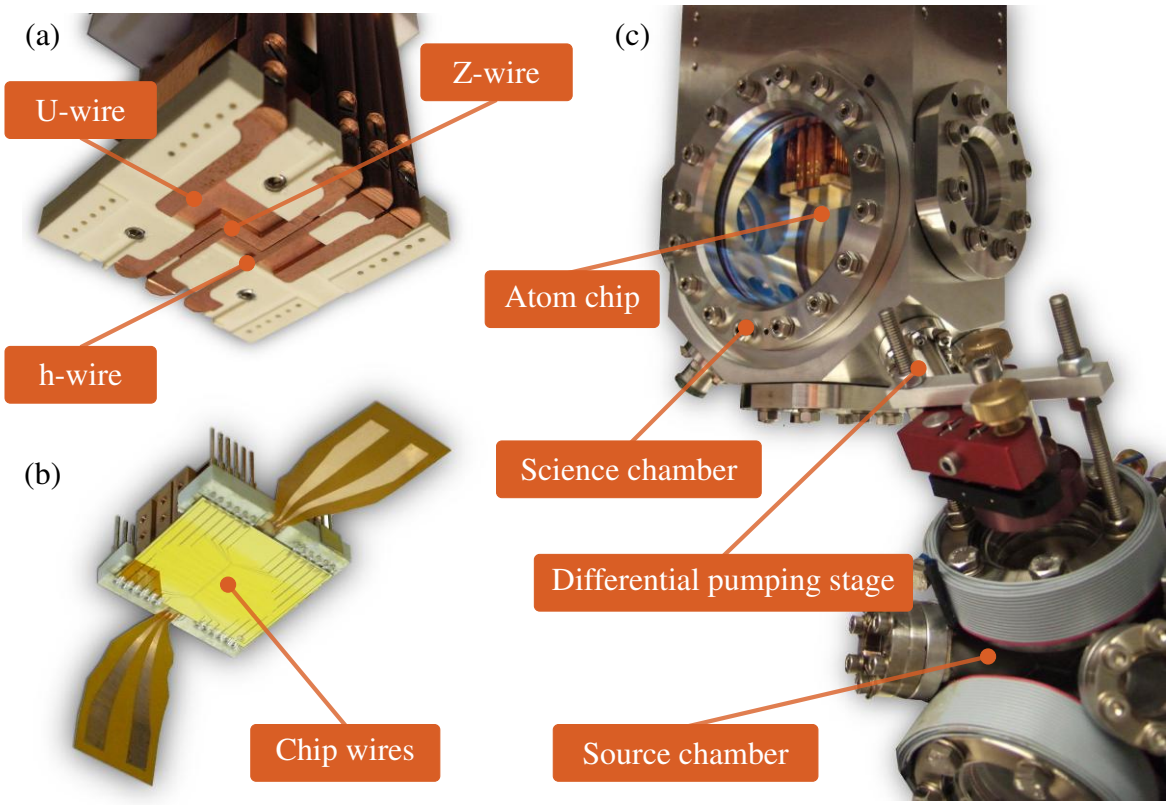

Fig. 3.1 In (a) the macroscopic copper wire structures are visible. The atom chip is mounted above these wires (b) and placed in the science chamber as shown in (c). Atoms are optically transported from the source chamber to the science chamber via a push beam. In the science chamber they are trapped in a quadrupole trap formed by the macroscopic U-wire and bias coils. The Z-wire and the h-wire are then used to load the atoms in the chip trap, which is formed by chip wires and has a much smaller volume compared to the MOT trap.

- **Atom chip trap:** Micro fabricated wires on the chip surface along with an external bias field can realize Ioffe-Pritchard traps with different aspect ratios (figure 3.2). The typical trapping frequencies for the elongated harmonic trap are $\omega_{\parallel} = 2\pi \cdot 10\,\text{Hz}$ and $\omega_{\perp} = 2\pi \cdot 2\,\text{kHz}$.

3.2.2 Radio Frequency (RF) Traps

Applying near-field rf-fields, a wide range of trapping potentials can be realized on an atom chip. The interaction between the atoms and the rf-field, leads to new dressed eigenstates which are superposition of the original Zeeman levels. If the rf-fields are turned on adiabatically, the atoms follow the new eigenstates. Because the level structure of the atoms is

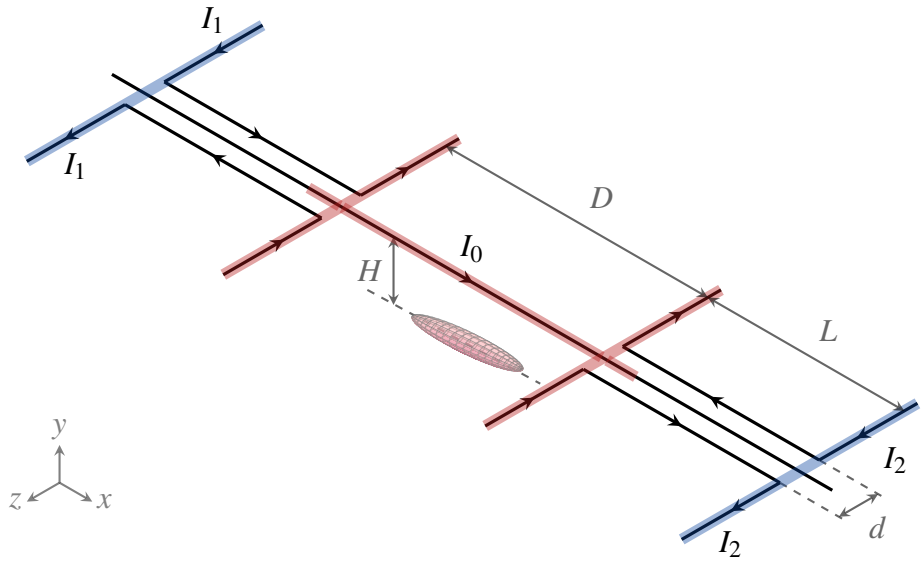

Fig. 3.2 The wires forming the chip trap and the cigar-shaped atomic cloud (not to scale) are shown above. Two pairs of U-shaped wires along with a guide wire and an external bias field produced by a Helmholtz coil realize a Ioffe-Pritchard trap. $D = 1900\,\mu\text{m}$, $L = 1400\,\mu\text{m}$ and $d = 250\,\mu\text{m}$, hence the wires are effectively forming an H-shaped trap, highlighted in red in this figure. The wire segments highlighted with blue are far away from the center of the trap, thus their contribution is negligible. Two U-shaped wires in each pair carry the same current. The current of the guide wire, I_0 and each U-pair, I_1 and I_2 can be tuned independently. The ratio I_2/I_1 determines the position of the trap along the x-direction. The vertical distance of the cloud to the chip can be adjusted by the external bias field and the current passing through the guide wire, I_0.

now tunable by rf-radiation, new trapping potentials such as a double well potential can be realized.

The two rf-wires are oriented parallel to the guide wire and placed between the guide and the U-wires (not shown in figure 3.2).

3.3 Experimental Cycle

Repeatability and robustness are essential features of chip experiments. For many measurements, large statistics are key, so a short cycle time is desirable. Here, a typical experimental cycle is listed:

1 **Collection** (10 s) The vapour generated by a rubidium dispenser is gathered, cooled down, and transported to the science chamber by the double MOT system shown in figure 3.1.

2 Molasses (7 ms) For a short time, the magnetic fields are turned off and the atoms are cooled down to 50 µK via sub-Doppler cooling.

3 Optical pumping (0.5 ms) An optical pumping pulse is applied to prepare the atoms in the maximally stretched $|F = 2, m_F = 2\rangle$ state, which is a low-field seeking state.

4 Intermediate trapping stage (6 s) The macroscopic Z- and h-wire produce a Ioffe-Pritchard trap to load the chip. Evaporative cooling starts at this stage, which can cool the atoms down to 3 µK.

5 Loading the chip trap (0.5 s) In this stage the macroscopic trap is slowly turned off and the chip trap is ramped up. During the loading, the evaporative cooling is paused. At the end of this stage, the magnetic trap is merely created by the chip wires along with the external bias coils, discussed in figure 3.2.

6 Further evaporative cooling in the chip trap ($1.4 - 1.9$ s) Evaporative cooling is continued in the chip trap. In the end, a 1d quasi-condensate is obtained with up to ten thousand atoms at $15 - 150$ nK.

7 Manipulation ($0 - 500$ ms) Depending on the experimental requirements, further manipulation can be performed, for example by applying rf-fields.

8 Detection The trap is switched off and the cloud falls under gravity. The atomic density is measured using absorption imaging which cause the atoms to be scattered away. With this, an experimental cycle is completed.

The process is organized and controlled via a real-time control system using AdWIN and MATLAB [33, 34].

Chapter 4

One-Dimensional Beam Shaping

Beam shaping, i.e. producing arbitrary intensity profiles, is necessary in order to realize arbitrary optical dipole potentials as discussed in 2.2. In our particular case beam shaping along a single spatial dimension is needed. To realize this, the intensity (or the phase) of the light field has to be modified using a spatial light modulator (SLM). There are different kinds of SLMs to choose from. Our choice fell on the Digital Micromirror Device (DMD) which is a reflective SLM.

This chapter starts with a brief motivation, why 1d beam shaping is important in our experiment. Afterwards, an introduction to DMDs is given, the tool with which 1d beam shaping can be performed. In this part, the specifications of the DMD used in our setup are presented in detail. The chapter continues with clarifying, how a 1d arbitrary potential can be obtained by imaging a 2d binary pattern. In this regard, the connection between the formation of an optical dipole potential and the properties of a 1d quasi-condensate is discussed. Then, the means by which grayscales can be obtained is introduced. Finally, the theoretical basis for spatial filtering with a so called 4-f imaging system is provided.

4.1 Motivation

The dynamics of a 1d quasi-condensate depends on the 1d trapping potential. In atom chip experiments, Maxwell's equations and the wire geometry are a strong constrains which make the realization of arbitrarily adjustable magnetic potentials very difficult. Moreover, the imperfection of micro wires on the chip which is due to the limitations of nano fabrication technology causes potential roughnesses [35]. In figure 4.1 the 1d density profile of a thermal cloud trapped in a potential made by imperfect wires is shown. In this measurement, the U-shaped micro wires on the chip (see figure 3.2) are turned off, so without any imperfection in micro wires the potential and therefore the 1d density profile would be flat. These

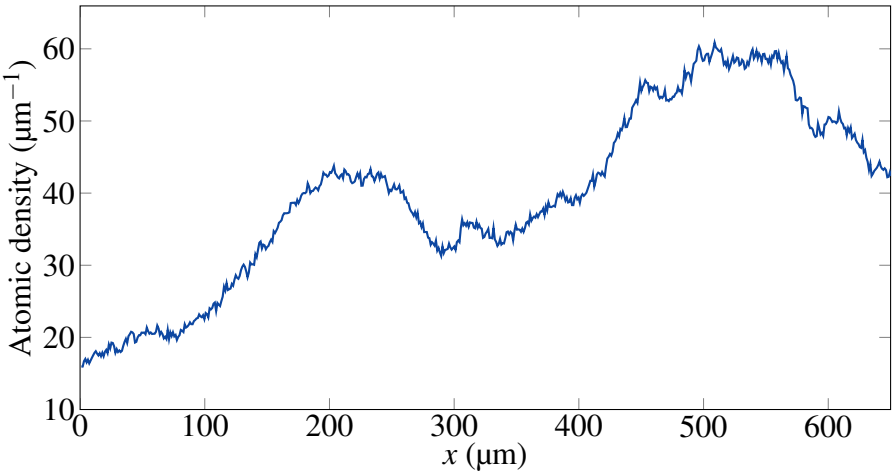

Fig. 4.1 Trapping a thermal cloud in the magnetic potential created by wires with imperfections. The linear atomic density along the longitudinal axis is plotted for a thermal cloud 2 ms after expansion. In this measurement the U-shaped wires on the chip, providing the longitudinal confinement, are turned off so that the trapping potential along x-axis is purely created by the wire imperfections

inhomogeneities in the atomic density can mask interesting physics which can be investigated having a homogeneous density distribution [36]. In principle, realizing optical dipole potentials can overcome both these limitations. With arbitrary 1d optical dipole potentials, in addition to magnetic confinement, many interesting trapping potentials can be realized, by above all a flat box-shaped potential which allows for a homogeneous atomic density in the trap.

4.2 Digital Micromirror Device (DMD)

Invented by solid state physicist and Texas Instruments[1] (TI) Fellow Emeritus Dr. Larry Hornbeck in 1987 [16], a DMD is an array of hundred thousands of individually addressable micromirrors (pixels). Each of these mirrors can be tilted along a fixed axis and stay in one of two mechanical stable states denoted as ON or OFF. DMDs are widely used in projectors, television devices and optical metrology. High speed, stability and high controllability, make a DMD an ideal candidate to be used as a SLM to produce arbitrary optical dipole potentials.

DMDs differ in resolution, pixel size, maximum pattern refresh rate and the illumination wavelength range. In this work a DLP9500 DMD from TI (shown in figure 4.2) is used, which has 1920×1080 (FullHD) micromirrors, each being a $10.8 \times 10.8\,\mu$m square. For this

[1] http://www.ti.com/

(a) (b)

Fig. 4.2 Pictures of our DMD. (a) The DMD is connected to an aluminum plate. This plate fits into the black ionized mount shown in picture. In our setup, the DMD is mounted upright. (b) The logo of the Atominstitut of the Vienna University of Technology is projected by DMD.

device, the maximum pattern refresh rate in FullHD is about 18 kHz. However, it can also be used in an area of interest (AOI) mode, in which the maximum pattern rate increases dramatically. For example, the maximum pattern rate goes up to 47.6 kHz for an AOI of 1920×200 pixels. This is particularly interesting for 1d beam shaping, where only a narrow region on the DMD chip is illuminated. In the DLP9500 DMD, mirrors are tilted about the diagonal and the two stable states are defined to be at $\pm12^\circ$. It is common to mount the DMD at a 45° angle to keep all optical axis in one plane parallel to the optical table. However, in our case, this makes it impossible to take advantage of the AOI mode. In our setup, the DMD is mounted upright, as shown in figure 4.2. Our DLP9500 DMD extension board is part of the V-9501 module from ViALUX[2]. This module also contains a V4395 main board and its powerful controller suit, APL-4.3. ViALUX provides a user-friendly API (application programming interface) with a variety of examples to start with. The DMD can also be

[2]ViALUX is an authorised value-added reseller and Design House partner for the Texas Instruments' DLP®Discovery™ line of micro mirror arrays.

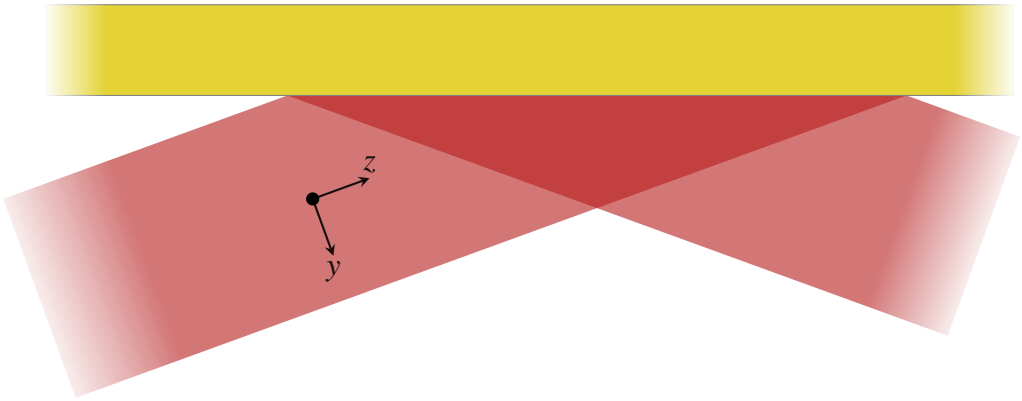

Fig. 4.3 Scheme of the dipole light incidence on the atom chip. The black dot, represents a 1d quasi-condensate formed below the atom chip (yellow). The x-axis runs along the cloud and is pointing out of the plane of paper. Because the entrance window to the vacuum chamber is tilted, the light is propagating in the z-direction at an angle to the chip surface and is reflected from it. The 2d image of the DMD, $I(x,y)$, is formed in the xy-plane at the position of the atoms ($z = 0$). Because the width of the cloud along y is smaller then the resolution of the optical system, only the central slice of the image is seen by the atomic cloud, namely $I(x,0) \equiv I(x)$. As the light reflects from the chip, there is always a region where the incident beam and the reflected beam are interfering. To avoid this interference at the position of the cloud, the size of the beam in y-direction has to be small enough.

externally triggered in order to synchronize the optical dipole trapping process with other parts of an experimental cycle.

Due to the small size of the mirrors, a DMD acts as a 2d reflective grating which reflects coherent light in many different diffraction orders [38]. The saw-tooth-like structure arising from the tilted mirrors can be described as a blazed grating with the blaze angle θ_B being the tilt angle of the mirrors. This angle is optimized to separate the light path in the ON and OFF states of the mirror. The incident angle under which the maximum intensity is diffracted in a desired angle (i.e. the optical axis of the following imaging system) is defined by the wavelength of the light, the blaze angle, and the mirror size.

For beam shaping, the DMD can either be imaged directly or in the Fourier plane, the former being more straightforward and more efficient if phase modulation of the light field is not necessary. In experiments which are using holography to build dipole traps [39, 40], the DMD is used in the Fourier plane of the optical system in order to perform phase modulations. In our experiment however, the exact modulation of the intensity is of primary importance, so the DMD is imaged directly with an optical system, discussed in chapter 5.

4.3 One-Dimensional Optical Dipole Potential

Imaging the DMD pattern results in a 2d intensity distribution $I(x,y)$ in the plane of atoms (see figure 4.3). For a 1d quasi-condensate in a harmonic trap with transversal frequency $\omega_\perp$, the width of the cloud can be estimated by $\sqrt{\hbar/M\omega_\perp}$, which is the width of the Gaussian ground state wave function of the radial trap [32]. In the experiment, typical values for $\omega_\perp$ lie between 1.4 to 2.1 kHz which leads to a width smaller than 300 nm. This value is smaller than the resolution of any optical system including the one introduced in chapter 5. This means that a single spot is larger than the vertical cloud extension so that only a tiny slice from the image, $I(x) \equiv I(x, y = 0)$, is relevant for the optical dipole trapping, assuming that the cloud is at $y = 0$.

In the rest of this manuscript, $I(x)$ refers to a 1d intensity profile in the longitudinal direction.

4.4 Grayscaling

The DMD is a powerful device in terms of controllability and speed of performance, but ultimately, it can only produce binary patterns, which makes arbitrary beam shaping impossible. A way to get around this restriction is to use time and/or spatial averaging.

Time Averaging

Making use of the concept of time-averaged potentials [41], fast intensity modulations by the DMD can be exploited to gain grayscales. This modulation has to be so fast that only an average of it can be seen by atoms. Quantitatively, this means that the frequency of modulations has to be much higher than the trap frequency of the tight transverse confinement, $\omega_\perp \simeq 2\pi \cdot 2\,\mathrm{kHz}$, which defines the shortest dynamical time scale in the experiment. In the AOI mode of the DMD where less than hundred rows are addressed, the mirror states can be switched with a frequency of about 50 kHz. With such a modulation, at least four steps of grayscales can be achieved as explained in figure 4.4.

Spatial Averaging

Another method to gain grayscales is to design the optical system in a way that more than one binary pixel contributes to the intensity of one single spot in the image plane. The easiest way to do so is to use a demagnifying optical system in which a certain number of DMD pixels are mapped down to a single spot in the image plane as shown in figure 4.5.

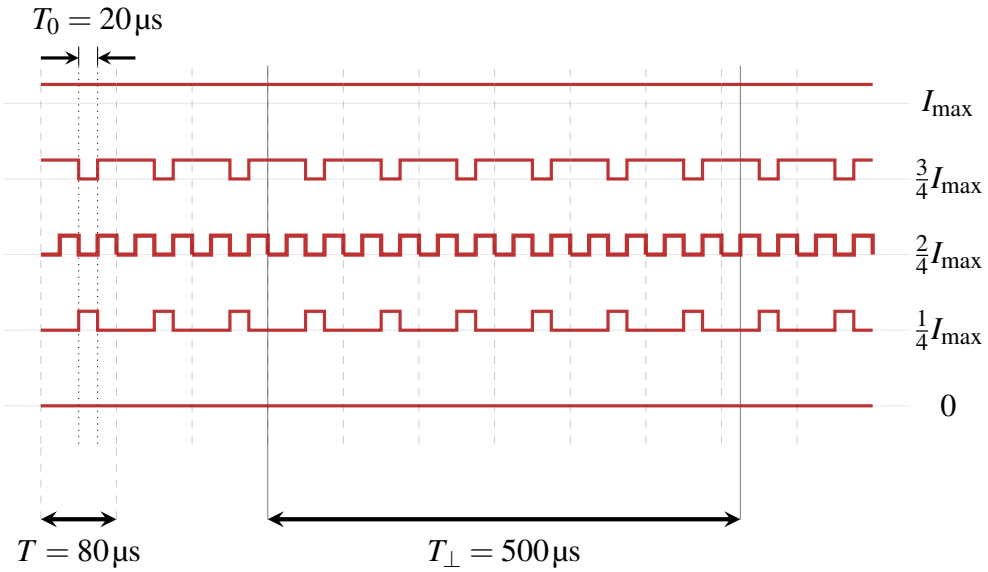

Fig. 4.4 Obtaining grayscales using the concept of time averaging. Five different time configurations for a single mirror are shown in each row. The horizontal axis is the time axis on which three important time scales are defined. $T_\perp$ is the shortest dynamical time scale of the experiment which is associated with the transversal trap frequency $\omega_\perp = 2\pi/T_\perp$. T_0 is the shortest time interval in which the state of a DMD mirror can be changed between the two stable states. T is a time scale which is "much" shorter than $T_\perp$, such that only an average of modulations can be seen by atoms within this time scale. In the top row, the mirror is always ON, hence the maximum intensity is seen by the atomic cloud. In the last row, the mirror is always OFF, so the resulting intensity is zero. Without time averaging, only these two binary cases can be realized. Exploiting the modulations within T, three different grayscales can be realized between the two limits.

Spatial filtering is another way to spatially average over a number of binary pixels. This can be performed by means of a 4-f imaging system described in the next section.

4.5 4-f Imaging System

A 4-f imaging system [42] is a two-lens focused imaging system in which the distance between the two lenses is the sum of their focal lengths, $f_1 + f_2$ as shown in figure 4.6. The magnification of such system is given by $m = f_2/f_1$. The outstanding advantage of this system is that a mask can be used in the Fourier plane in order to selectively filter out Fourier components of the object pattern. Considering this system as an isoplanatic two-dimensional linear system [43, 44], the output (image) function $g_{out}(x,y)$ is given by the convolution of

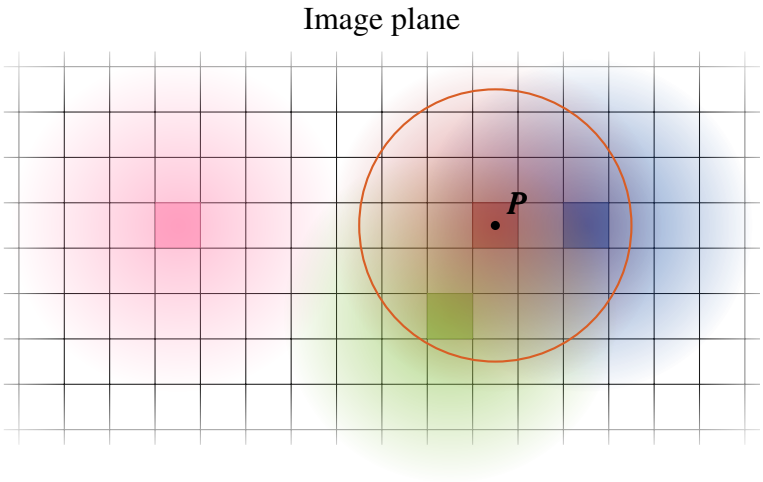

Fig. 4.5 Obtaining grayscales using the concept of spatial averaging. The DMD chip is shown in the image plane of an optical imaging system. If there were no diffraction, any pixel could be resolved perfectly in the image plane and if four pixels (shown in different colors) were switched on, only one of them (the red) pixel would contribute to the intensity of point P. In the real world however, the image of a pixel is blurred due to the diffraction. Each pixel is now imaged as a broad spot, whose size depends on the resolution of the optical system. In this case all pixels within the orange circle contribute to the intensity of point P, including the blue and the green colored pixels.

the input (object) function $g_{\text{in}}(x,y)$ and the point-spread function $h(x,y)$,

$$g_{\text{out}}(x,y) = \iint_{-\infty}^{+\infty} h(x-x',y-y')\, g_{\text{in}}(x',y')\, dx'\, dy' \ , \tag{4.1}$$

which according to the convolution theorem, can also be written as

$$G_{\text{out}}(\nu_x,\nu_y) = H(\nu_x,\nu_y)\, G_{\text{in}}(\nu_x,\nu_y) \ . \tag{4.2}$$

Here $G_{\text{out}}(\nu_x,\nu_y)$ and $G_{\text{in}}(\nu_x,\nu_y)$ are the Fourier transforms of $g_{\text{out}}(x,y)$ and $g_{\text{in}}(x,y)$ respectively and the so called transfer function, $H(\nu_x,\nu_y)$ is the Fourier transform of $h(x,y)$. In the Fourier plane, the spatial frequencies (ν_x,ν_y) are related to the spatial coordinates via $(x = \lambda f_1 \nu_x, y = \lambda f_1 \nu_y)$, where λ is the wavelength of the imaging light. For a mask with transmittance $p(x,y)$ placed in the Fourier plane of a 4-f system, the transfer function has the convenient form,

$$H(\nu_x,\nu_y) = p(\lambda f_1 \nu_x, \lambda f_1 \nu_y) \ . \tag{4.3}$$

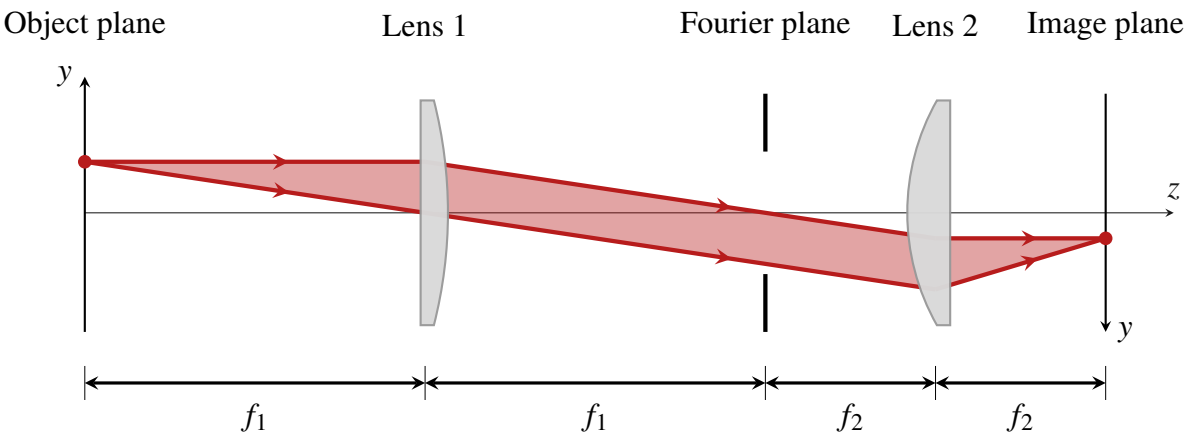

Fig. 4.6 Scheme of a demagnifying 4-f imaging system. The z-axis is the optical axis. f_1 and f_2 are the focal lengths of lens 1 and lens 2 respectively and $f_1 > f_2$, hence the system is demagnifying. In the Fourier plane, a mask with transmittance function $p(x,y)$ can be placed to manipulate the Fourier components of the object pattern which are obtained via a Fourier transformation by the first lens. The second lens, performs an inverse Fourier transformation on the resulting Fourier pattern and builds an inverted image in the image plane.

So for a 4-f imaging system the relation between the output and the input functions is simply determined by the shape of the mask in the Fourier plane,

$$G_{\text{out}}(\nu_x,\nu_y) = p(\lambda f_1 \nu_x, \lambda f_1 \nu_y)\, G_{\text{in}}(\nu_x,\nu_y)\ . \tag{4.4}$$

Given an input function, $g_{\text{in}}(x,y)$, and a certain mask with transmittance $p(x,y)$, the intensity distribution function of the output, $I(x,y) = |g_{\text{out}}(x,y)|^2$, can be easily calculated using equation (4.4). This simplicity is particularly useful when simulating the whole system numerically. If no mask is present, $p(x,y)$ is set by the size of the smaller lenses.

Choosing different masks one can perform spatial filtering in different ways such as low-pass, high-pass or horizontal-pass filtering. The later, which leaves Fourier components in the horizontal direction unchanged so that the resolution along this axis is not altered, is the most interesting for us as will be described in the next section.

4.5.1 Grayscaling using Spatial Filtering

Spatial filtering is one of the means by which spatial averaging of a binary pattern can be realized. Manipulating the Fourier components of a pattern only in y-direction will change the properties of the image only in this direction. To build arbitrary 1d potentials a horizontal slit can be used to block the high frequency components in y-direction and make the contribution

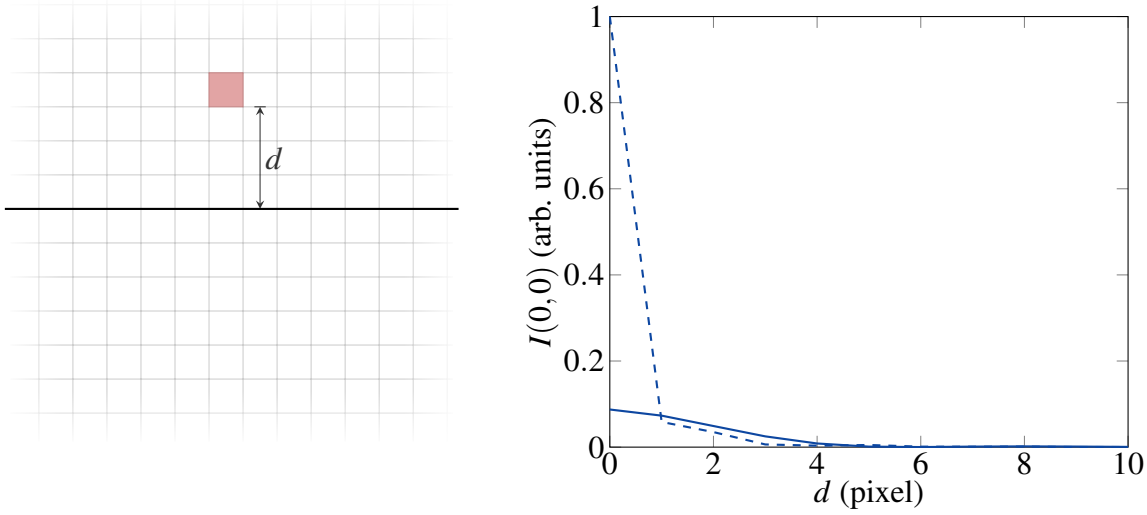

(a) (b)

Fig. 4.7 Realization of spatial averaging using spatial filtering. (a) Scheme of the central part of the DMD chip. The solid horizontal line is the middle line. The red pixel is ON (i.e. reflecting light into the imaging optics) and the rest is OFF. The configuration shown in (a) is used as the binary function for simulating a 4-f system with two different masks in Fourier plane. (b) The intensity in the center of image, $I(0,0)$, is plotted for different distances d. The dashed curve is for the case in which the rectangular aperture is totally open in both directions ($l_x, l_y = 12\,\text{mm}$). The solid curve represents the case in which the aperture is totally open in x-direction but only slightly open in y-direction ($l_x = 12\,\text{mm}$ and $l_y = 3\,\text{mm}$). As the intensity quickly drops to zero in the first case, only two levels of grayscale can be obtained, namely the maximum intensity and zero. In the second case the intensity gradually decreases, making grayscaling possible.

range of a pixel in this direction longer. Due to the blocking of Fourier components, there is a trade off between power loss and the length of the contribution range which will be shown later in this section (see figure 4.7).

In this following, a series of numerical simulations are presented, to achieve a deeper understanding of a 4-f system and how it can be used in 1d arbitrary beam shaping. In these simulations the intensity distribution function of the image $I(x,y)$ is calculated for a given input function $g_{\text{in}}(x,y)$ and a transmittance function $p(x,y)$.

Assuming that the DMD pattern is given by a binary function $b(x,y)$ and that the DMD is illuminated by a beam which has an intensity distribution function $l(x,y)$, the input function is given by $g_{\text{in}}(x,y) = b(x,y)l(x,y)$.

If the DMD is illuminated by a Gaussian beam which has its maximum at (x_c,y_c), $l(x,y)$ can be written as

$$l(x,y) = A\exp(-2\frac{(x-x_c)^2}{w_x^2} - 2\frac{(y-y_c)^2}{w_y^2}) \,, \tag{4.5}$$

where A is an arbitrary amplitude and w_x and w_y are the $1/e^2$ widths of the beam in vertical and horizontal direction respectively.

For a rectangular aperture of width l_x and height l_y which has an offset x_0 and y_0 with respect to the x- and y-axis respectively, the transmittance function $p(x,y)$ has the form

$$p(x,y) = \begin{cases} 1 & \text{if } |x-x_0| < l_x \text{ and } |y-y_0| < l_y \\ 0 & \text{otherwise} \end{cases} \,, \tag{4.6}$$

or equivalently

$$p(\lambda f_1 \nu_x, \lambda f_1 \nu_y) = \begin{cases} 1 & \text{if } |\nu_x - x_0/\lambda f_1| < l_x/\lambda f_1 \text{ and } |\nu_y - y_0/\lambda f_1| < l_y/\lambda f_1 \\ 0 & \text{otherwise} \end{cases} . \tag{4.7}$$

In the numerical simulations, a 4-f system with $f_1 = 300\,\text{mm}$ and $f_2 = 100\,\text{mm}$ is simulated and the wavelength of the light is set to be $\lambda = 660\,\text{nm}$. For the rectangular aperture, l_x and l_y is set to be between 0 to 12 mm, which is given by the real adjustable aperture in the experimental setup (see 5.2).

To show how horizontal-pass filtering can be exploited to gain grayscales in a 1d profile, consider the configuration shown in figure 4.7a. Here a pixel which has a distance d to the center of the DMD is turned on. For this configuration the intensity is calculated with two different transmittance functions. In the first case the rectangular slit is totally open (l_x, $l_y = 12\,\text{mm}$) and in the other one, the slit is totally open in x-direction and only slightly open in y-direction ($l_x = 12\,\text{mm}$ and $l_y = 3\,\text{mm}$). In figure 4.7 the intensity in the center of image, $I(0,0)$, is plotted for different distances. The plot shows that for the first case, as the pixel is shifted up only by one pixel, the intensity in the center of the image drops to near zero. For larger distances, the pixel does not contribute to the intensity of the center of the image. For the second case however, the intensity is decreased slowly and it goes to zero at $d = 50$ pixels. In this case, more levels of grayscale are available as in the first case, where only two levels of grayscales is obtainable. Note that because the slit is always totally open in x-direction, shifting the superpixel horizontally leads to results similar to the dashed line in figure 4.7 for both cases. This independence makes 1d beam shaping possible and convenient for such optical systems. The downside of the spatial filtering is also apparent

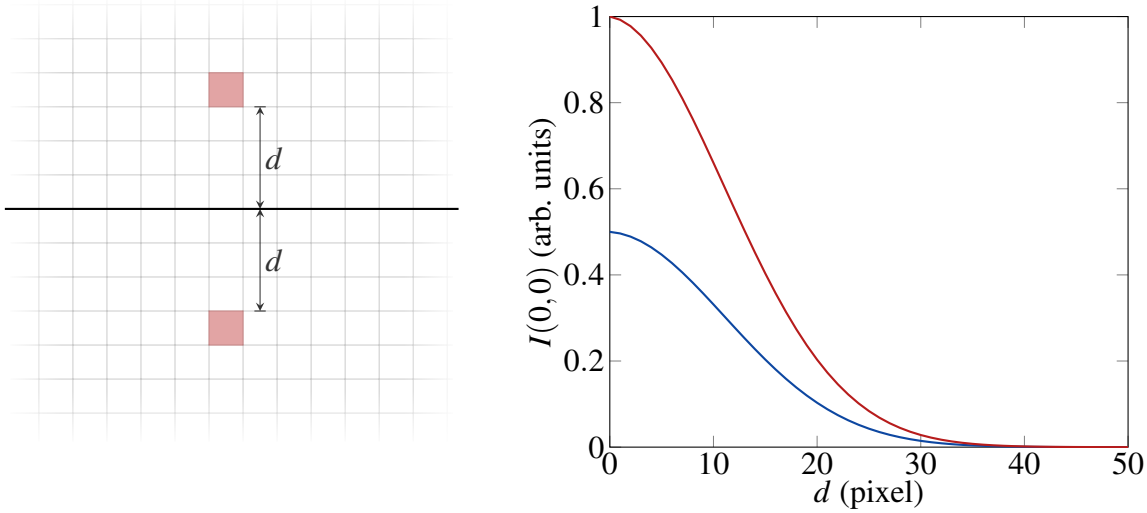

(a) (b)

Fig. 4.8 Interference effects in spatial filtering. (a) Scheme of the central part of the DMD chip. The solid horizontal line is the middle line. The two pixels shown in red are ON (i.e. reflecting light into the imaging optics) and the rest is OFF. (b) The intensity in the center of the image, $I(0,0)$, is plotted for different distances d. Simulating the configuration in (a), the red curve is the intensity in the center of the image for different values of d. The blue curve is obtained by simulating each of the two pixels independently and then adding the calculated intensities. Both curves are normalized to the maximum value of the red curve. In the simulations, the rectangular aperture is totally open in x-direction but only slightly open in y-direction ($l_x = 12\,\text{mm}$ and $l_y = 0.3\,\text{mm}$) and is placed symmetric with respect to the optical axis. ($x_0, y_0 = 0$)

in figure 4.7b. As both curves are normalized to the dashed curve, the transmitted intensity from the partially closed aperture is considerably lower.

Although realizing an arbitrary 1d intensity profile is in principle achievable using spatial filtering, it is more complicated than figure 4.7 might suggest. The challenge is that the contribution of two pixels in the intensity can not be easily added due to interference effects. To understand this, consider another pixel below the center of the DMD which is also located at a distance d from the center. In figure 4.8, the intensity $I(0,0)$ is plotted as a function of d for two different cases. In the first case, $I(0,0)$ is calculated for the two pixels independently and then added together and plotted as the blue curve in figure 4.8. In the second case both superpixels are imaged simultaneously and the $I(0,0)$ is plotted as the red curve for different distances. At each distance d, the pattern with two pixels has a different periodicity in comparison to the pattern with a single pixel. As a consequence, the power distribution of

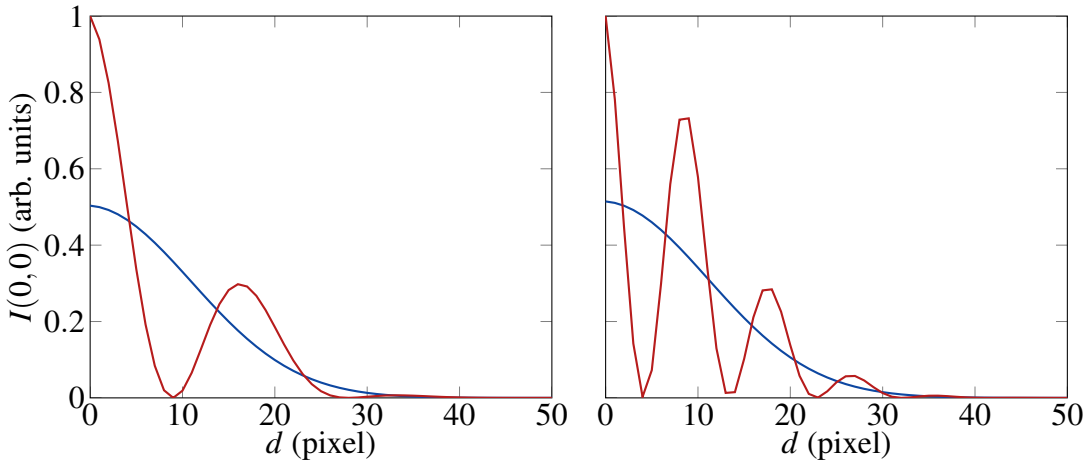

(a) (b)

Fig. 4.9 Interference effects caused by asymmetric apertures. In each plot, the intensity in the center of the image, $I(0,0)$, is plotted for different distances d. Simulating the configuration in 4.8a, the red curve is the intensity in the center of the image for different values of d. The blue curve is obtained by simulating each of the pixels independently and then adding the calculated intensities. Both curves are normalized to the maximum value of the red curve. In the simulations, the rectangular aperture is totally open in x-direction but only slightly open in y-direction ($l_x = 12\,\text{mm}$ and $l_y = 0.3\,\text{mm}$) and is placed asymmetrically with respect to the optical axis, (a) $x_0 = 0$ and $y_0 = 0.5\,\text{mm}$, (b) $x_0 = 0$ and $y_0 = 1\,\text{mm}$

the Fourier components is different and ultimately, the spatial filtering has different impact on the resulting image for each pattern.

There is also another degree of complexity regarding horizontal-pass filtering. In all the simulations so far, the aperture was symmetric with respect to the optical axis, i.e. $y_0 = 0$. Figure 4.9 shows that effects of interference can even more strongly appear in a system with an asymmetric aperture. Considering all aspects of spatial filtering, it turns out that it is a complicated, yet feasible method to gain grayscales. The number of grayscales which can be realized is proportional to the power loss due to the filter in Fourier plane.

Chapter 5

Optical Setup

The optical setup used to image the pattern on the DMD chip onto the plane of the atoms, consists of three main parts. In the so called beam preparation part, the polarization and the shape of the beam are modified, before it illuminates the DMD chip. After reflecting from the DMD, a 4-f system serves as the first demagnification stage and also as the spatial filtering of the pattern. In the second demagnification stage, a single plano-concave lens is coupled to the transverse imaging system (TIS) [31, 45] via a polarizing beam splitter (PBS) cube. Along with the objective of the TIS, it forms another demagnifying imaging system. The first two parts, including the DMD, are mounted on a separate breadboard while the third part is installed on the breadboard of the TIS.

Each of these three main parts are discussed in detail in this chapter.

5.1 Beam Preparation

In this initial stage, shape and polarization of the illumination beam are adjusted so that the maximum power of the beam can be used in trapping. Wavelength of this light is $\lambda = 660\,\text{nm}$. A schematic of the setup is shown in figure 5.1.

As mentioned before, the optical trap imaging system is coupled to the TIS via a PBS in the parallel part of the TIS as shown in figure 5.6. In the beam preparation setup, an initial $\lambda/2$ wave plate and a PBS cube are used to obtain a clean linearly polarized beam. An additional $\lambda/2$ wave plate is then used to adjust the polarization of the beam such that it passes through the coupling PBS with minimal losses.

To monitor the power stability, a small fraction of the light ($\approx 1\%$) is reflected to a photodiode by a beam sampler. The signals from this photodiode can be used along with an AOM (acousto-optic modulator) after the laser system to build a feedback loop to smooth out

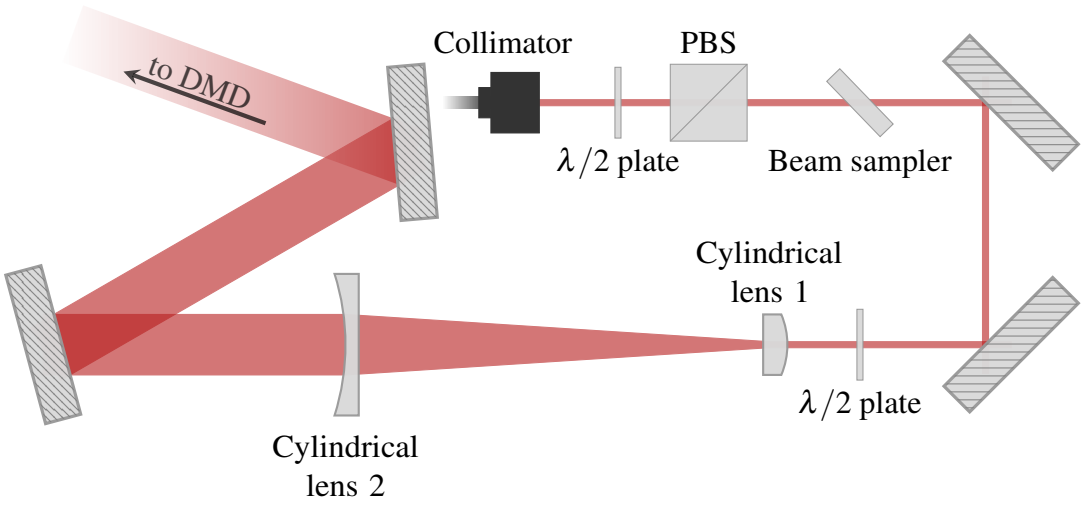

Fig. 5.1 Scheme of the beam preparation setup (not to scale). The beam coming out from the collimator (Schäfter+Kirschhoff 60FC-4-A6.2S-02) is a linearly polarized single mode Gaussian beam with a $1/e^2$ diameter of 0.9 mm. The wavelength of the trapping light is $\lambda = 660$ nm provided by an "opus 660" diode laser from Laser QUANTUM. The first $\lambda/2$ wave plate rotates the polarization of the beam such that it passes through the PBS cube with minimal loss. This will guarantee that the light going through the next $\lambda/2$ wave plate is linearly polarized with a fixed orientation. This second wave plate is used to adjust the polarization such that the beam can be totally reflected in the PBS coupling the dipole trap light into the TIS (not shown here). The beam sampler reflects about 1% of the light to a photodiode to monitor the power stability. Two cylindrical lenses (Thorlabs LK1426L1-B and LJ1558RM-B) are used as a beam expander which expands the beam in one direction and let it unchanged in the other.

intensity fluctuations due to the laser system and the polarization drifts in the optical fiber which are converted to intensity fluctuation by the PBS.

To make an elongated optical trap, it is sufficient to illuminate only a few rows of the DMD. Illuminating rows which are always off causes unwanted power loss. An elongated Gaussian beam is formed by a beam expander formed by two cylindrical lenses as shown in figure 5.1. After the second cylindrical lens, the beam has a $1/e^2$ thickness of 1.1 mm and is 10 mm broad.

As mentioned in 4.2, the DMD is mounted upright. Since the mirrors are tilted diagonally, in order to have the reflected beam perpendicular to DMD surface, the incident beam can not be parallel to the breadboard. Therefore the last two mirrors in the setup, shown in figure 5.1, are mounted in different heights, to adjust the incident angle.

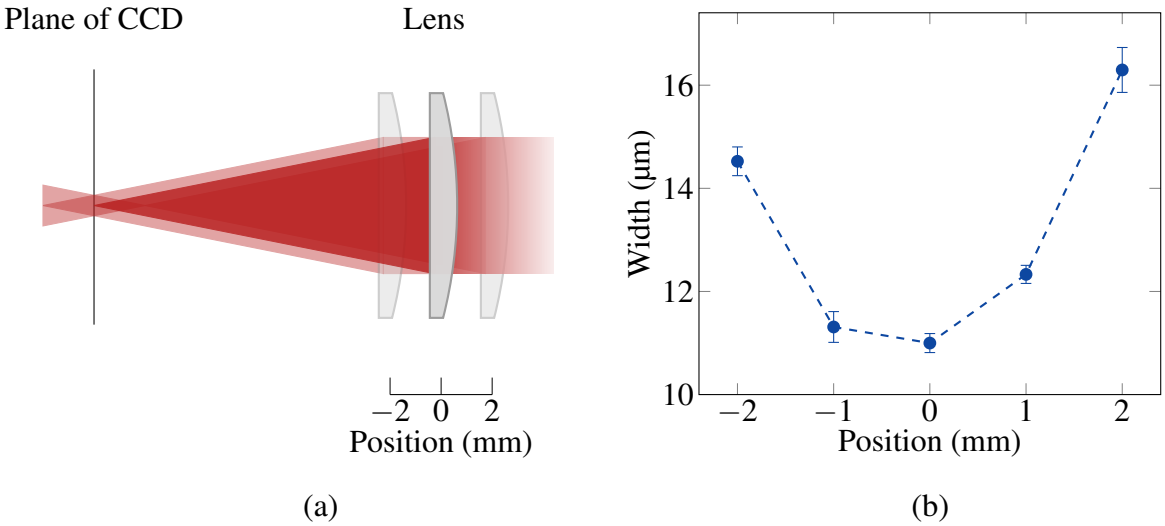

(a) (b)

Fig. 5.2 Finding the focus of the first lens in the first demagnification stage. (a) The procedure is shown schematically (not to scale). The lens is placed at different positions and the width of the Gaussian beam on the CCD chip is measured. (b) The measured widths are plotted at different positions.

5.2 First Demagnification Stage

A 4-f system with $f_1 = 300\,\text{mm}$ and $f_2 = 100\,\text{mm}$ is used as an initial three-fold demagnification stage. Horizontal-pass filtering is performed in this system using a rectangular slit, whose width in the horizontal and vertical direction can be adjusted independently from 0 to 12 mm.

5.2.1 Alignment

The DMD mount shown in figure 4.2 is designed in a way that the DMD can be replaced by a camera such that the CCD chip is at the same position as the DMD chip. To align the 4-f system a collimated Gaussian beam is focused onto the CCD chip via the first lens. In order to set the focal point of the first lens in the plane of the DMD chip, the $1/e^2$ width of the Gaussian beam is measured as a function of distance between the lens and the CCD chip (see figure 5.2). In this configuration the light takes the revers path through the first lens compared to the final setup.

For a collimated beam, a 4-f system acts as a beam expander which expands or shrinks the beam size by a factor m. Having a collimated input beam, the distance between the two lenses in a beam expander can be aligned by checking the collimation of the output beam. If the distance between the lenses is $f_1 + f_2$, the output beam will be a collimated beam. As the

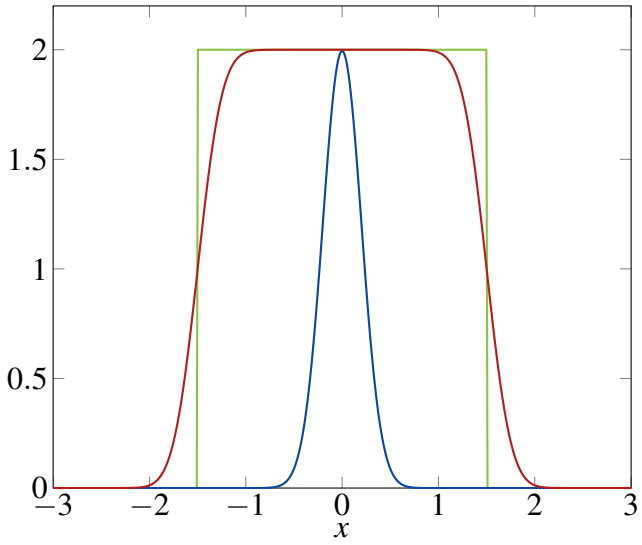

Fig. 5.3 Convolution of a box car function with a Gaussian function. The red curve is the convolution of the box car function shown in green with a normalized Gaussian function represented by the blue curve. The width of the Gaussian function is $w = 0.2$ and for the box car function $M = 2$, $L = 3$ and $c = 0$.

position of the first lens is already fixed, a collimated input beam is used to align the second lens. This lens is placed such that the output beam be collimated.

5.2.2 Resolution and Demagnification

Assuming a Gaussian point-spread function (psf),

$$h(x) = \frac{1}{w\sqrt{2\pi}} \exp\left(-\frac{x^2}{2w^2}\right), \tag{5.1}$$

the resolution of the optical system in each direction can be defined as the $1/e^2$ width w, of this function in that direction.

To measure this width, an n×n superpixel on the DMD is imaged. In 1d, this superpixel can be represented by a box car function

$$g_{\text{in}}(x) = \begin{cases} M & \text{if } |x-c| < L/2 \\ 0 & \text{otherwise} \end{cases}, \tag{5.2}$$

which has the value M between $x = c - L/2$ and $x = c - L/2$ and vanishes elsewhere.

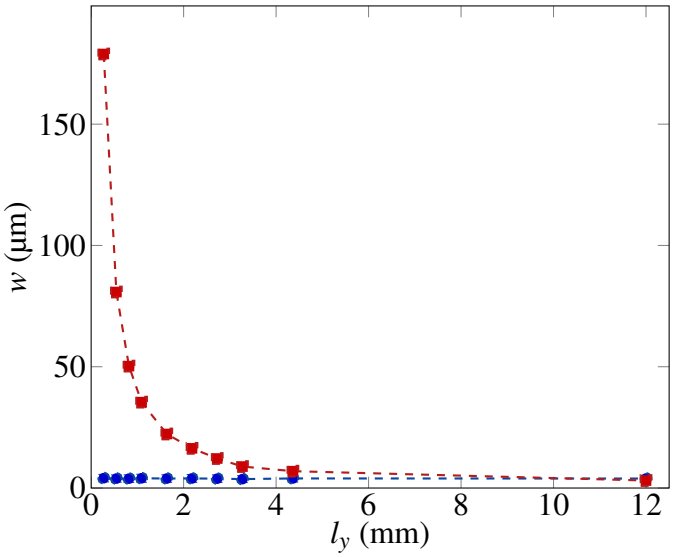

Fig. 5.4 Resolution of the first demagnification stage in x- and y-direction. The width of the Gaussian point spread function is obtained by fitting the function $|g_{\text{out}}|^2$ on the integrated 1d intensity profiles of images of a 8×8 superpixel in x- and y-direction independently. The blue and the red curve represent the resolution in x- and y-direction respectively. This figure shows that the resolution in x-direction is unchanged as the width of the slit

According to equation 4.1, the image function g_{out} is given by

$$g_{\text{out}}(x) = g_{\text{in}}(x) * h(x) \tag{5.3}$$

$$= \frac{M}{2}\left[\text{erf}\left(\frac{x+c-L/2}{w\sqrt{2}}\right) - \text{erf}\left(\frac{x+c+L/2}{w\sqrt{2}}\right)\right]. \tag{5.4}$$

The resolution in x and y-direction can be obtained by fitting $|g_{\text{out}}|^2$ to integrated 1d intensity profile in each direction with a fixed superpixel size L.

In figure 5.4, the resolution in x- and y-direction is plotted as a function of the slit width in y-direction. It is clear from the figure that the width of the slit in one direction has no influence in the resolution in the other direction. This is already discussed as an advantage for 1d beam shaping in 4.5. The resolution in the x-direction in this measurements is $w = 4.2 \pm 1.6\,\mu\text{m}$. The error represented is the fit error which is relatively large due to the relatively large camera pixel size ($3.75\,\mu\text{m}$), that is very close to the resolution of the optical system.

Demagnification of the system is obtained by comparing the size of a 100×100 superpixel and its image on the CCD chip and is calculated to be $m = 3.01$.

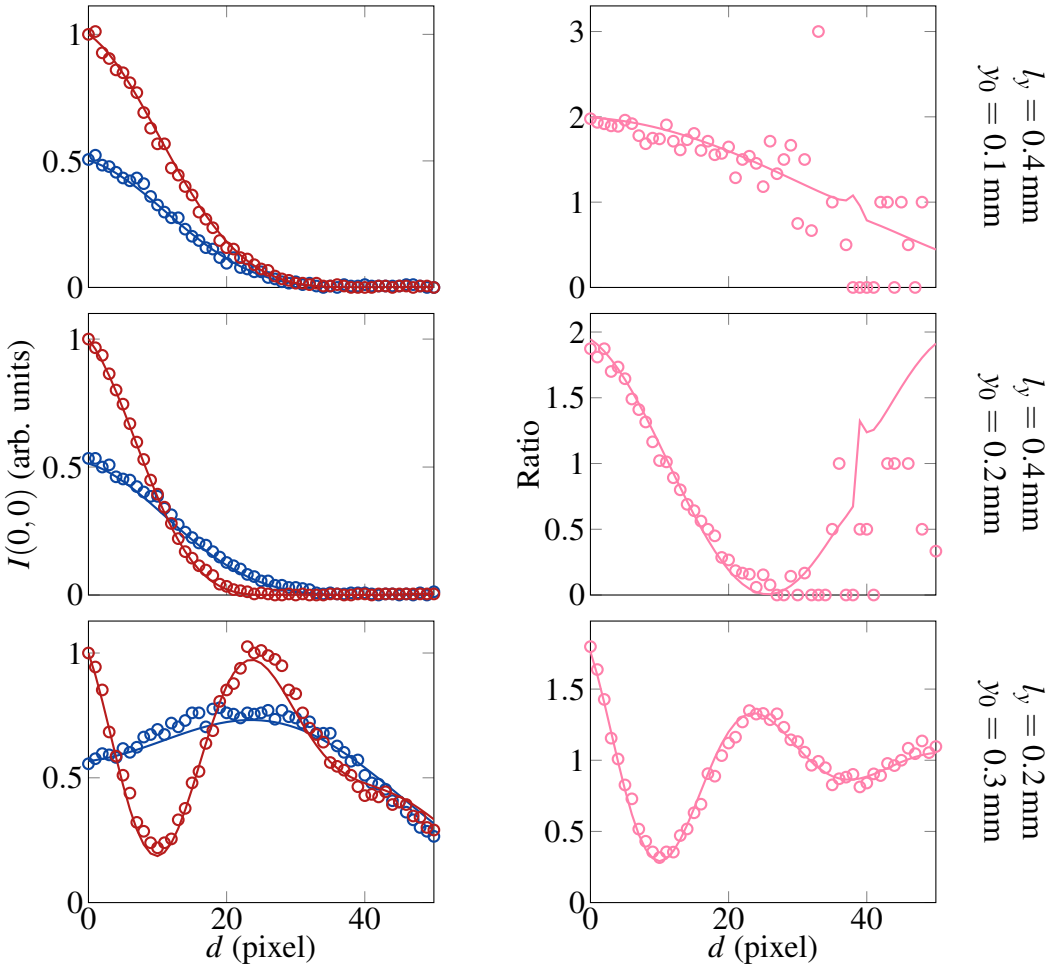

Fig. 5.5 Experimental observation of the interference effects in spatial filtering. In the left column, the intensity in the center of the image, $I(0,0)$, is plotted for different distances d (see figures 4.7 & 4.8). The circles represent the measured data and the curves are fits obtained by numerical simulations. Realizing the configuration in 4.8a (but with a 6×6 superpixel instead of a single pixel), the red circles are the intensity in the center of the image for different values of d. The blue circles are obtained by imaging each of the superpixels independently and then adding the measured intensities. In each plot of the left column, both blue and red circles are normalized to the value of the red data for $d = 0$. In all three measurements the rectangular aperture is totally open in x-direction ($l_x = 12\,\mathrm{mm}$) but only slightly open in y-direction. For each set of data, the l_y and y_0 values are extracted from the fits. The plots on the right column are the ratio of the red circles/curves to blue circles/curves. In the two upper plots, as the measured intensities go to zero, the error in the ratio increases. In the last row, an offset of the Gaussian beam caused the peak in the intensity measurements.

5.2.3 Grayscaling

The results of the simulations discussed in 4.5 can be confirmed experimentally. The configurations demonstrated in figures 4.7a and 4.8a are realized experimentally with a minor difference. Instead of a single pixel, a 6×6 superpixel is imaged to suppress the effect of the camera pixel size.

The results are presented in figure 5.5 which suggests that the pixels which are vertically far from the center can be used to gain grayscales. The number of obtainable grayscales depends on the width of the rectangular aperture in the vertical direction (l_y). The smaller the width, the more grayscales can be produced. However this is limited by the power loss due to the spatial filtering.

The observed behaviour points to the fact that even when ignoring the power issues and the interferences due to the spatial filtering in vertical direction, the interference effects between neighbouring pixels in x-direction represents an obstacle to deterministically achieve arbitrary 1d intensity profiles.

Width and Offset of the Rectangular Aperture

By fitting the numerical simulations to the measured data, important information can be read out as the width of the rectangular aperture (l_x, l_y) and its offset from the optical axis (x_0, y_0) can be determined. As show in figure 4.9 and 5.5, the offset has a great impact on the form of interference on the center of the pattern. Since the width of the slit can not be determined by the mechanics of the rectangular aperture, this measurements can be used to adjust the width as well as the offset.

5.3 Second Demagnification Stage

The image formed by the first demagnification stage is now the object of the second demagnification stage shown in figure 5.6. In this system, a plano-convex lens and the high-NA[1] objective of the TIS ($NA = 0.27$) image the pattern onto the plane of atoms. A PBS cube is used to couple the dipole trap light into the TIS. The imaging beam ($\lambda = 780\,\text{nm}$) is p-polarized and therefore passes through the PBS, while the dipole trap light is s-polarized so that the PBS reflects it into the TIS objective. In an experimental cycle, the imaging starts after all the trapping potentials, including the dipole potential, are turned off.

Although coupling the dipole trap optics to the TIS allows for utilizing a high-NA objective, the downside is that the wavelength of the trapping light is then limited by the

[1] Numerical aperture

coatings of the optical elements in the TIS which does not allow for wavelengths below 650 nm.

5.3.1 Alignment

The initial alignment of the second demagnification stage can be done by using the system in reverse as an absorption imaging system and focusing the picture of the atom cloud on the CCD replacing the DMD. Because the objective as well as the two lenses in the first demagnification stage are all fixed, Lens 3 has to be shifted in order to obtain a sharp image of atoms. The fine adjustment can be performed with the DMD and the TIS by looking at density patterns written into large clouds by the DMD setup.

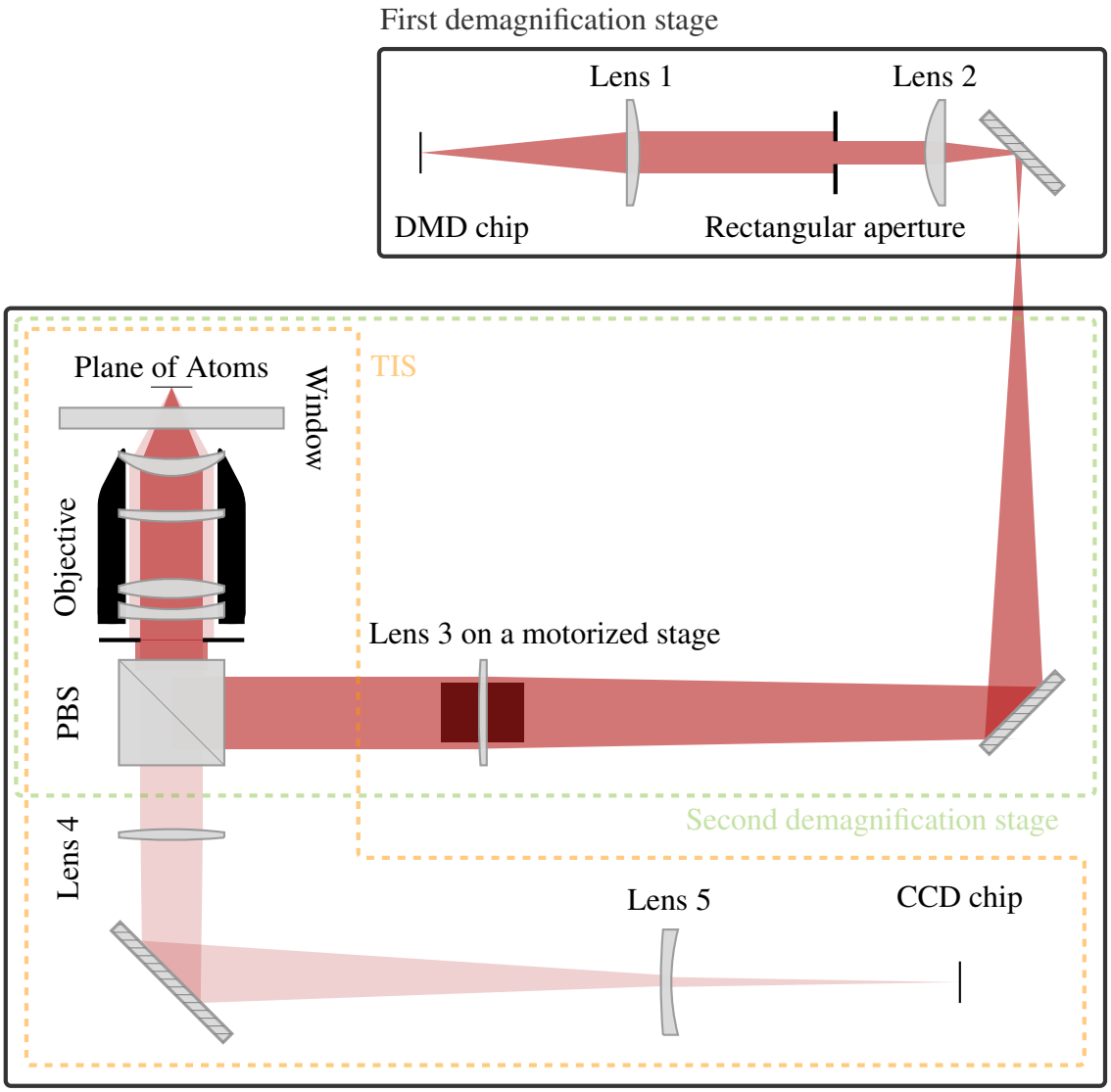

Fig. 5.6 Scheme of the first and the second demagnification stage and the TIS (not to scale). Each solid frame indicates a separate breadboard. In the first demagnification stage, lens 1 (LA1256-B) along with lens 2 (LA1050-B) forms a 4-f system which is connected to the second demagnification stage by two mirrors. The first mirror is a backside polished mirror, behind of which an overview camera can be placed. Lens 3 (LA1727-B, all three lenses from Thorlabs) with the objective of the TIS forms the second demagnification stage. This lens can be shifted with a motorized stage to adjust the focus of the whole system in the plane of atoms. While the p-polarized imaging light, $\lambda = 780\,\mathrm{nm}$ (shown in pink) passes through the 2-inch PBS cube, the s-polarized optical trap light, $\lambda = 660\,\mathrm{nm}$ (shown in red) is reflected into the objective of TIS. Note that the cube is placed in the parallel part of both second demagnification stage and TIS. The imaging beam is focused on the CCD chip via lens 4 and lens 5 that form a telephoto group to shrink the size of the optical system.

Chapter 6

Designing and Optimizing One-Dimensional Potentials

In the two previous chapters, the basic concepts and tools related to 1d beam shaping were introduced and discussed in detail. The topic of this chapter is, how these tools can be utilized to realize an arbitrary 1d potential.

According to equation 2.13, the 1d optical dipole potential experienced by the atoms is proportional to the 1d intensity profile which is formed by the image of the DMD pattern on the plane of atoms, as explained in 4.3 . Thus, to obtain an arbitrary 1d potential, the 2d binary pattern of the DMD has to be properly designed.

In this chapter, first, a probabilistic optimization method to design 2d DMD patterns is introduced. The method is then applied to three different 1d target intensity profiles based on simulated feed back process. Finally, an optimization process based on experimental feedback is discussed.

6.1 Designing a 2D Pattern

The ultimate goal of designing the 2d pattern on the DMD is to obtain a 1d intensity profile $I(x)$, which is as close as possible to the target intensity $I_{\mathrm{t}}(x)$. Considering an area of interest (AOI) on the DMD with $n_x \times n_y$ pixels, $2^{(n_x \times n_y)}$ different patterns (states) can be realized. The problem is to find the pattern which minimizes the "energy" function $E(x) = |I(x) - I_{\mathrm{t}}(x)|$. Testing all patterns to find the best one in a brute force approach is impossible. Even for a small AOI with $n_x = 20$ and $n_y = 10$ pixels, the phase space is astronomically large with $2^{200} \approx 10^{60}$ states. Many algorithms exist to solve minimization problems with large state

spaces, such as neural networks or genetic algorithms. An easy to implement, yet reliable method is simulated annealing[1] [46].

In the following, first, a brief introduction to simulated annealing and the algorithm used for pattern optimization is given. Then the results of numerical simulations for three different target 1d potentials are presented. Finally, the patterns are imaged via the first demagnification state (see 5.2) onto a CCD chip and the resulting 1d potentials are shown and discussed.

6.1.1 Simulated Annealing Algorithm

Simulated annealing is an iterative probabilistic searching algorithm, based on the Metropolis algorithm[2] [47], which finds the global optimum of a given energy function E for systems with large phase space $\{\psi_i\}$ approximately. Starting from an initial state, in each step, a neighbour state is chosen randomly to be compared with the current state of the system. Based on an acceptance probability $P(E_i, E_j, T)$, the new state will either be accepted or discarded. This probability depends on the energy of the current state, $E_i = E(\psi_i)$, the energy of the new neighbour state, $E_j = E(\psi_j)$, and the parameter T which is called "temperature". This temperature is the parameter regulating the probability of accepting neighbour states which are energetically unfavorable in comparison to the current state of the system. For lower temperatures, the acceptance probability for energetically unfavorable states decreases. The optimization starts at a high temperature to allow the system to go through the different parts of the phase space without getting stuck in local minima. The temperature is then decreased gradually, forcing the system to stay in the regions with smaller energies. For temperatures close to zero, accepting energetically unfavorable states is almost impossible. In this limit, the energy of the achieved state is approximately the global minimum of the energy function. A pseudocode of the algorithm is given in algorithm 1.

In a typical simulated annealing optimization problem, first, an initial state, ψ_i, and an initial temperature, T_i, have to be defined. This temperature is chosen regarding the energy scales of the system. If the initial temperature is chosen high enough, the initial state can be a randomly chosen state of the system. Another important choice is the annealing schedule, i.e. a plan to decrease the temperature in each step toward the final temperature T_f. The most straightforward way to perform this, is to divide the current temperature by a constant Λ, which is close to 1. For each scheduled temperature, the system must have enough time to

[1] The method is inspired by annealing in matallurgy, a technique involving heating a material above its recrystallization temperature and scheduled cooling to alter its physical or chemical properties.

[2] A Monte Carlo sampling algorithm, which yields sequence of random samples from a probability distribution. It is generally used for sampling from multi-dimensional distributions.

Initialization
$\psi \leftarrow \psi_\mathrm{i}$
Calculate $E = E(\psi)$
$T \leftarrow T_\mathrm{i}$
while $T > T_\mathrm{f}$ **do**
  for $j \leftarrow 1$ **to** M **do**
    Choose a neighbour state ψ'
    Calculate $E' = E(\psi')$
    Calculate $P(E, E', T)$
    Generate a uniformly distributed random number $r \in [0, 1)$
    if $r \leq P(E, E', T)$ **then**
      $\psi \leftarrow \psi'$
      $E \leftarrow E'$
    else
      The current state doesn't change.
    end
  end
  Decrease T (e.g. $T \leftarrow T/\Lambda$)
end

Algorithm 1: Simulated annealing

walk through the accessible phase space. To ensure this, the size of the system is usually a reasonable scale for the number of Monte Carlo (MC) steps, M. Last but not least, an acceptance probability function has to be defined. A commonly used acceptance probability is based on the Boltzmann factor,

$$P(E_\mathrm{i}, E_\mathrm{j}, T) = \min\left\{1, \exp\left(-\frac{\Delta E_\mathrm{j,i}}{T}\right)\right\}, \tag{6.1}$$

where $\Delta E_\mathrm{j,i} = E_\mathrm{j} - E_\mathrm{i}$. This function guarantees that all transitions with $\Delta E_\mathrm{j,i} < 0$ will be accepted, but not all energetically unfavorable transitions are thrown away. Depending on temperature, a transition with positive energy difference also has a chance to be accepted.

In the following, simulated annealing is used to design and optimize 2d DMD patterns which result in desired 1d intensity profiles.

2D Pattern Optimization using Simulated Annealing

For an AOI with $n_x \times n_y$ pixels, the phase space consists of all possible binary patterns which can be realized by these pixels, $\{b_\mathrm{i}(x, y)\}$. Defining a target function $I_\mathrm{t}(x)$, the energy of a

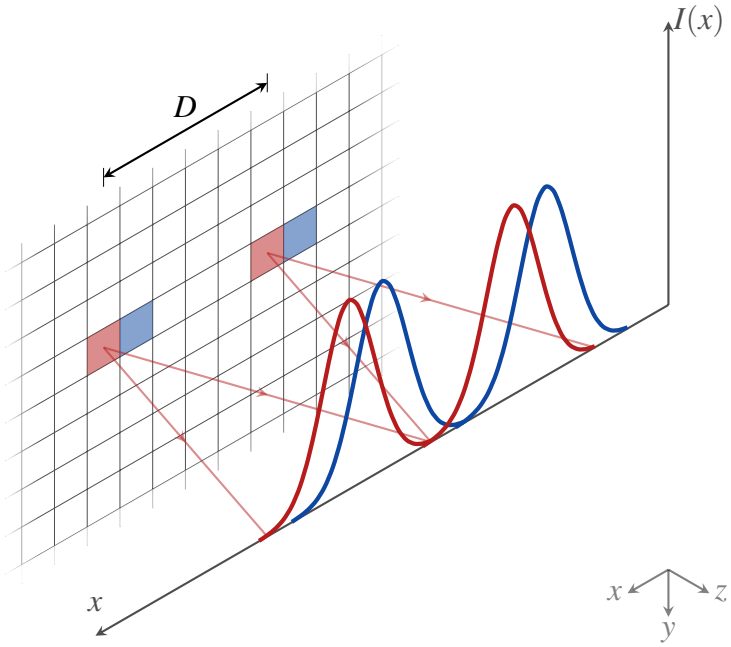

Fig. 6.1 Schematic showing the independent effect of pixels with large enough distances along x-axis. Here, it is shown that the resulting intensities of the two red pixels with distance D do not overlap. This holds for all pixels in these two columns. In an optimization process, the regions corresponding to these two columns can be handled independently. In each MC steps, a random pixel can be chosen in both of these two columns. Flipping the two chosen pixels, the energy can be calculated for the respective regions of influence and the decision making process can be independent. In the next MC step, the same process is repeated, but the random pixels are selected from the neighbouring columns in which the two blue pixels are shown. By shifting the columns in each step, the corresponding regions of influence are also shifted. The decision making in this step is based on the energy calculated for the new regions.

pattern $b_{\mathrm{i}}(x,y)$, is given by $E_{\mathrm{i}}(x) = |I_{\mathrm{i}}(x) - I_{\mathrm{t}}(x)|$. Here, $I_{\mathrm{i}}(x)$ is the 1d intensity profile in the image plane for $y = 0$, produced by the pattern $b_{\mathrm{i}}(x,y)$.

The initial temperature has to be set considering the energy scale of the initial state. The final temperature is a number very close to zero. At the end of an annealing step, the temperature is divided by Λ which is chosen between 1.01 to 1.1.

In a realistic situation in the experiment, the AOI has to contain up to $40 \times 300 = 12000$ pixels [3]. For such a large system, flipping only one pixel or even more pixels randomly to get to a neighbouring state is highly inefficient and requires very long simulation times to achieve decent results.

[3] $n_x = 300$ pixels on the DMD chip corresponds to a region of about 130 µm along the condensate

Because a single pixel on the DMD pattern only influences the intensity of a defined region on the image plane, many pixels can be flipped in one MC step and be independently accepted or rejected, providing the regions they act on do not overlap. The size of the region which is affected by a single pixel is defined by the point-spread function (psf) of the imaging system.

In the first demagnification stage of the optical system (see 5.2), horizontal-pass filtering results in a wide psf in vertical direction and a short psf in horizontal direction. Based on the resolution in the horizontal x-direction, a minimum distance D between pixels in this direction can be defined such that their corresponding spots in the image plane do not overlap (see figure 6.1). The energy function for flips in pixels further apart than D can therefore be calculated individually and used for decision making process of the related pixel.

Flipping many pixels simultaneously helps to speed up the optimization process but it does not mean that different regions can be optimized totally independently. The interferences due to the diffraction in the border of two regions distorts the optimization in the neighbourhood of the border.

In practice, in each MC step, a set of columns with distance D are selected. A random pixel is then chosen in each selected column. After flipping the elected pixels, the energy function of the new pattern has to be calculated separately for the region of influence of each column. This can be performed either by numerical simulations of a 4-f system, or via experimental realization. The acceptance procedure is carried out for each region individually, based on its energy difference. The accepted pixels stay flipped while the others are flipped back to their previous state. In the next MC step, the neighbouring column is selected and the whole process is repeated. Note that in each step not only the columns are shifted, but also the regions for which the energy is calculated. With this method, n_x/D uncorrelated pixels are flipped in each MC step and all n_x columns are scanned several times for $M \gg D$.

After the optimization, the root mean square (rms) of the relative deviation from the target intensity,

$$\varepsilon_{\mathrm{rms}} = \sqrt{\frac{1}{L}\int \left(\frac{I(x) - I_{\mathrm{t}}(x)}{I_{\mathrm{t}}(x)}\right)^2 dx}, \tag{6.2}$$

is defined as a measure for the quality of the obtained 1d intensity profile in a region of length L.

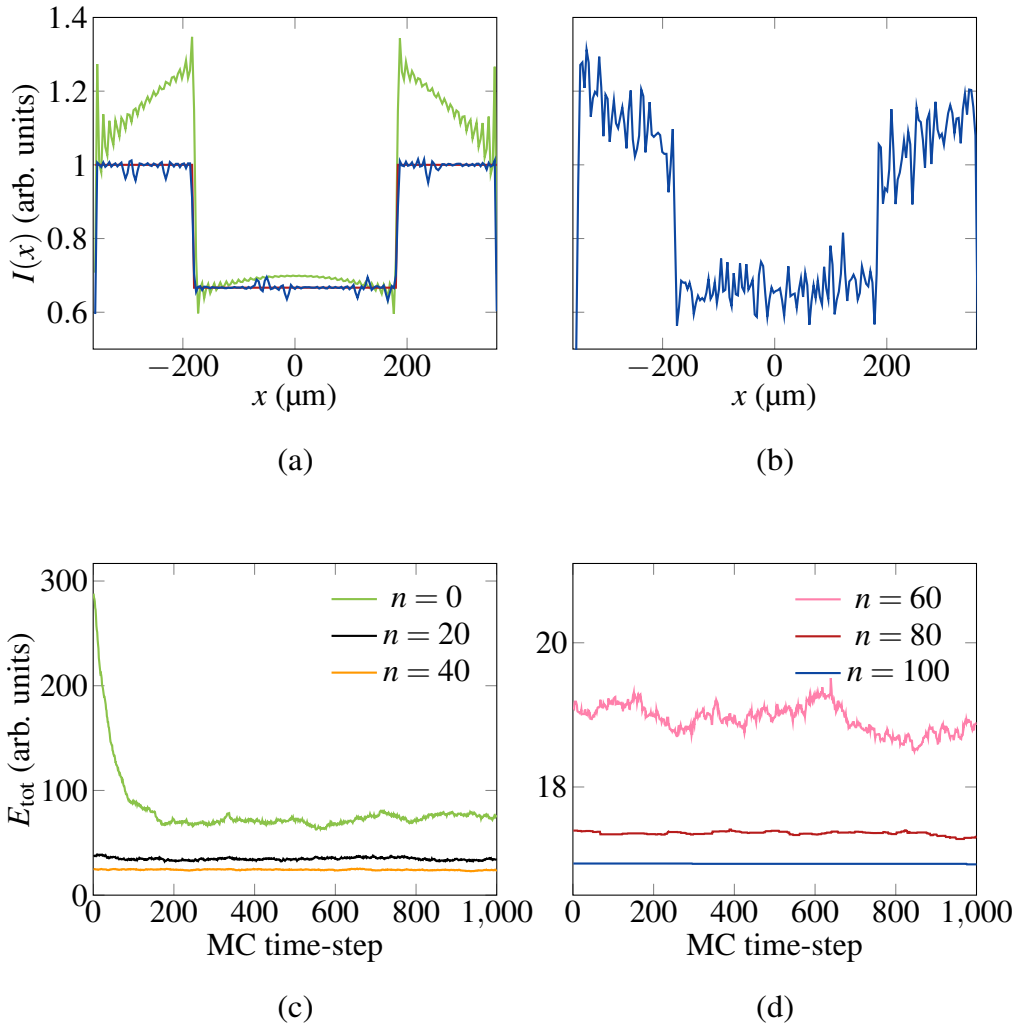

Fig. 6.2 Results of simulated pattern optimization of a box-shaped intensity profile using simulated annealing algorithm with parameters: $T_{\text{i}} = 5 \cdot 10^{-2}$, $T_{\text{f}} = 3 \cdot 10^{-4}$, $\Lambda = 1.05$ and $M = 1000$. The AOI on the DMD chip has $n_x = 200$ and $n_y = 150$ pixels. (a) The target intensity (red), initial intensity (green) and the final intensity profile (blue) are plotted for the region of interest. The rms error of the final profile in the central 360 µm region is $\varepsilon_{\text{rms}} = 1.77\%$. (b) The measured intensity profile after the first demagnification stage and the same rectangular aperture ($l_y = 0.4\,\text{mm}$, $y_0 = 0.2\,\text{mm}$). (c) & (d) The integrated energy in each MC step for different temperature stages $T_{\text{n}} = T_{\text{i}}/\Lambda^n$, with $n = 0$, 20, 40, 60, 80 and 100. The total energy converges as the temperature decreases. For the stage at T_{f}, the total energy does not change in 1000 MC steps which indicates that the system is reached a (local) minimum energy state. However, it can not be confirmed whether or not this state is the global minimum energy state.

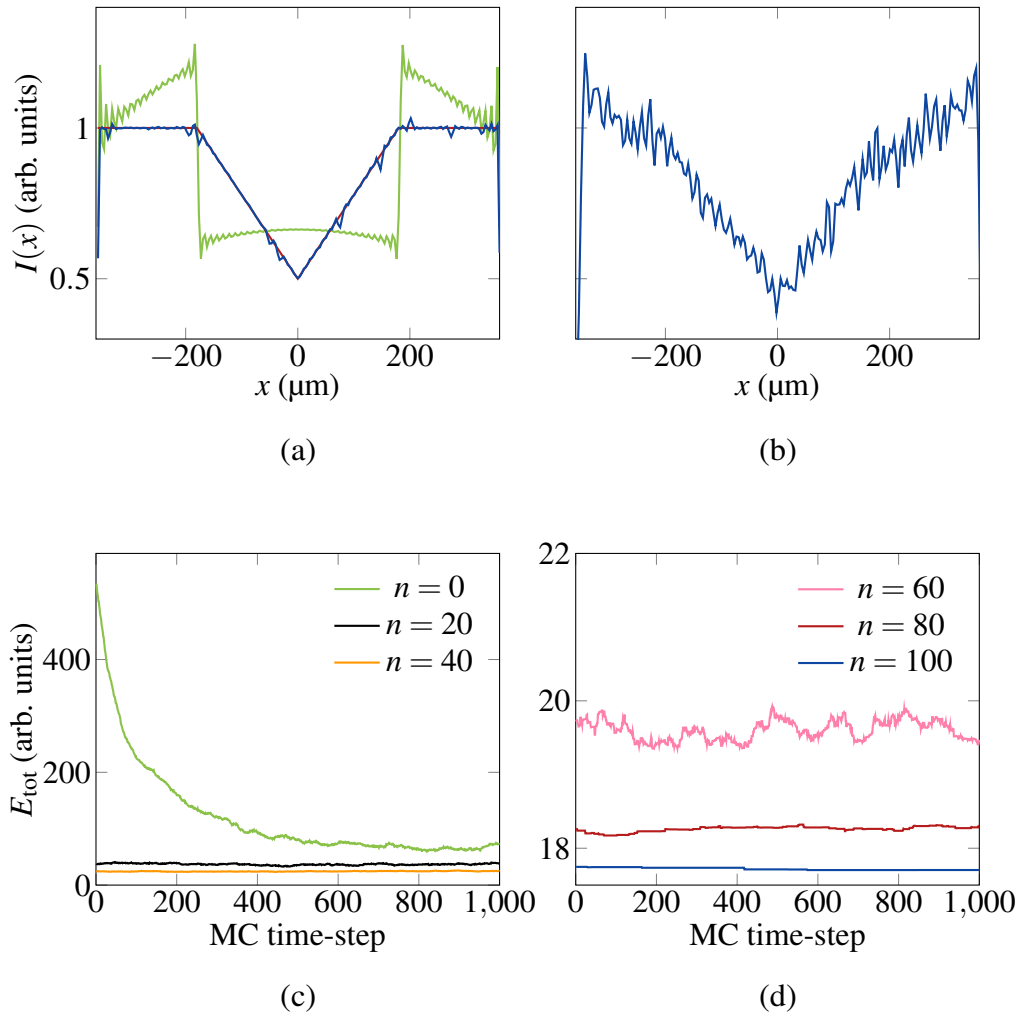

Fig. 6.3 Results of simulated pattern optimization of a V-shaped intensity profile using simulated annealing algorithm with parameters: $T_{\text{i}} = 5 \cdot 10^{-2}$, $T_{\text{f}} = 3 \cdot 10^{-4}$, $\Lambda = 1.05$ and $M = 1000$. The AOI on the DMD chip has $n_x = 200$ and $n_y = 150$ pixels. (a) The target intensity (red), initial intensity (green) and the final intensity profile (blue) are plotted for the region of interest. The rms error of the final profile in the central 360 µm region is $\varepsilon_{\text{rms}} = 1.36\%$. (b) The measured intensity profile after the first demagnification stage and the same rectangular aperture ($l_y = 0.4\,\text{mm}$, $y_0 = 0.2\,\text{mm}$). (c) & (d) The integrated energy in each MC step for different temperature stages $T_{\text{n}} = T_{\text{i}}/\Lambda^n$, with $n = 0$, 20, 40, 60, 80 and 100. The total energy converges as the temperature decreases. For the stage at T_{f}, the total energy does not change in 1000 MC steps which indicates that the system is reached a (local) minimum energy state. However, it can not be confirmed whether or not this state is the global minimum energy state.

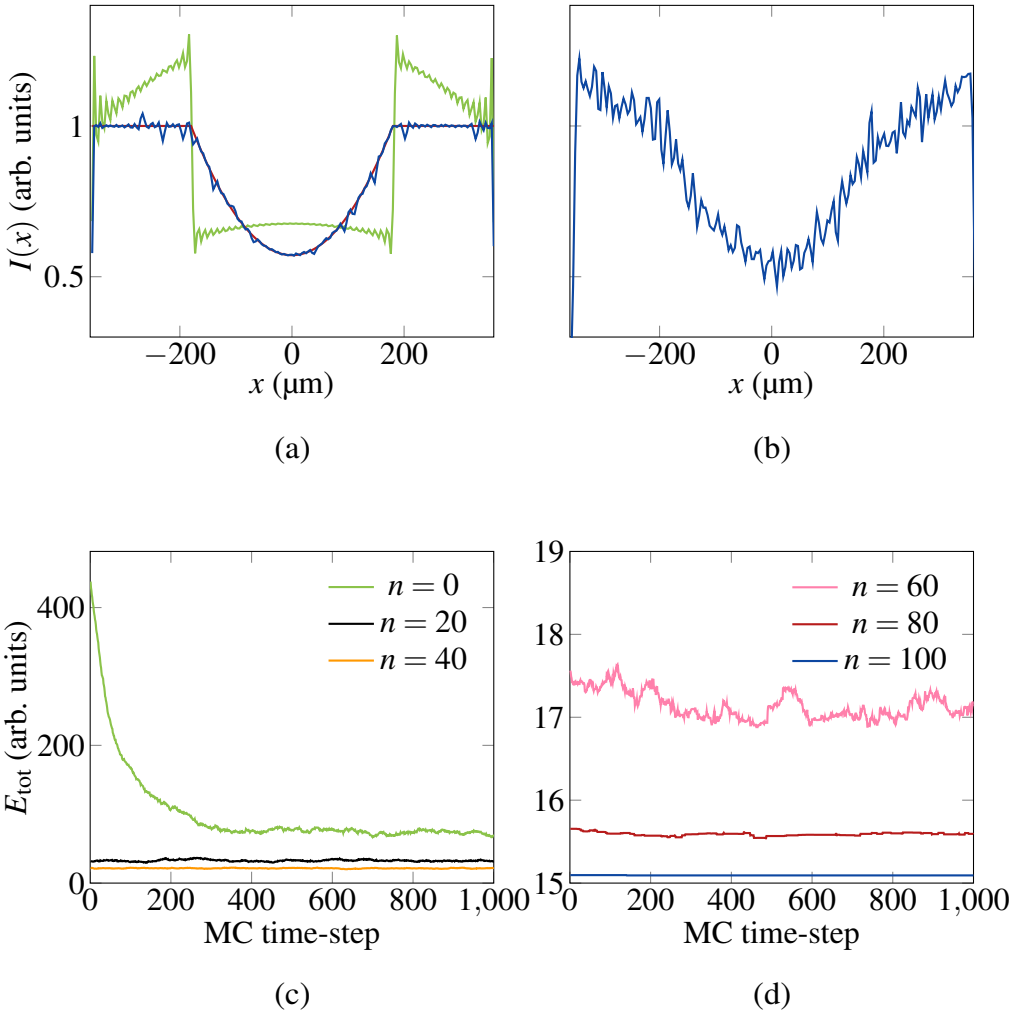

Fig. 6.4 Results of simulated pattern optimization of a harmonic intensity profile using simulated annealing algorithm with parameters: $T_{\text{i}} = 5 \cdot 10^{-2}$, $T_{\text{f}} = 3 \cdot 10^{-4}$, $\Lambda = 1.05$ and $M = 1000$. The AOI on the DMD chip has $n_x = 200$ and $n_y = 150$ pixels. (a) The target intensity (red), initial intensity (green) and the final intensity profile (blue) are plotted for the region of interest. The rms error of the final profile in the central 360 µm region is $\varepsilon_{\text{rms}} = 1.49\%$. (b) The measured intensity profile after the first demagnification stage and the same rectangular aperture ($l_y = 0.4\,\text{mm}$, $y_0 = 0.2\,\text{mm}$). (c) & (d) The integrated energy in each MC step for different temperature stages $T_{\text{n}} = T_{\text{i}}/\Lambda^n$, with $n = 0$, 20, 40, 60, 80 and 100. The total energy converges as the temperature decreases. For stage at T_{f}, the total energy does not change in 1000 MC steps which indicates that the system is reached a (local) minimum energy state. However, it can not be confirmed whether or not this state is the global minimum energy state.

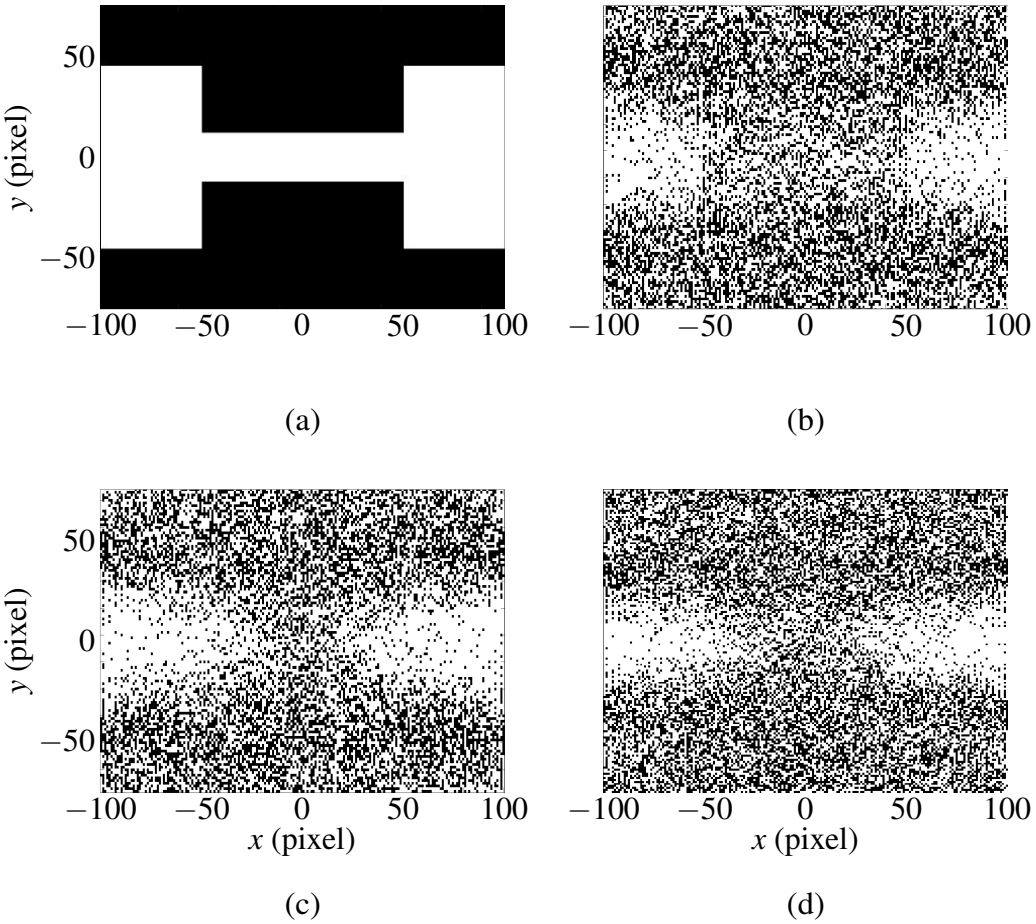

Fig. 6.5 2d DMD patterns in the AOI obtained at the end of the simulation process. (a) The initial pattern with which all the simulations were started. Final patterns for the box-shaped (b), the V-shaped (c), and the harmonic (d) target intensity profiles are shown as well. It is hard to read any information about the resulting 1d intensity profile from these patterns.

6.1.2 Examples

Using the method introduced in the previous section, pattern optimization is performed for an AOI with $n_x = 200$ and $n_y = 150$ for three different 1d target intensity profiles, namely a box-shaped, a V-shaped and a harmonic intensity profile (see figures 6.2a, 6.3a and 6.4a).

In the numerical simulations, the horizontal-pass filtering is performed by a slit with $l_x = 12\,\text{mm}$, $l_y = 0.4\,\text{mm}$ and $y_0 = 0.2\,\text{mm}$ (see figure 5.5). For all three targets, starting from an initial temperature T_i, the final temperature $T_\text{f} = 6 \cdot 10^{-3} \cdot T_\text{i}$ is achieved by dividing the temperature by $\Lambda = 1.05$ after each annealing step. The number of MC steps for each temperature is $M = 1000$.

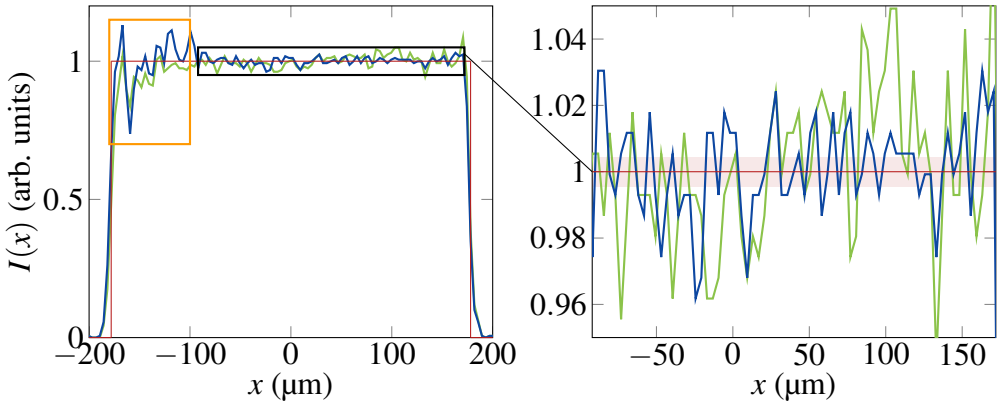

(a) (b)

Fig. 6.6 Result of pattern optimization with experimental feedback for a top-hat intensity profile using the simulated annealing algorithm at zero temperature with 100 MC steps. The AOI on the DMD chip has $n_x = 100$ and $n_y = 150$ pixels. (a) The target intensity (red), initial intensity (green) and the final intensity profile (blue) are plotted for the region of interest on the CCD. The rms error of the final profile is $\varepsilon_{\text{rms}} = 1.3\%$. (b) The region in the black frame is zoomed in. The interval shown in pink color indicates an averaged standard error of the measurement plotted in reference to the target due to the shot to shot fluctuations.

The initial and final 1d intensity profiles are plotted in figures 6.2a, 6.3a and 6.4a. For all three cases, ε_{rms} is less than 2% for the central region of final 1d intensity profile. The initial and final DMD patterns are shown in figure 6.5. The stochastic nature of the optimization process makes it hard to guess the resulting 1d intensity profile from looking at these patterns.

The total energy for six selected temperatures including the initial and final temperature is plotted in figures 6.2 to 6.4. For all three cases the total energy converged to a finite value at the final temperature. Although the value is small compared to the initial total energy, this does not necessarily mean that the final state corresponds to the global energy minimum.

In 6.2b, 6.3b and 6.4b, the final DMD patterns are imaged via the first demagnification stage of the optical setup with the same rectangular aperture parameters used in simulations. Because experimental effects such as aberrations, dust particles on the optical elements and inhomogeneities in the illumination beam are not included in the simulations, using the obtained patterns does not lead to the desired results in experiment. In order to realize arbitrary 1d intensity profiles, the optimization has to be performed using experimental feedback.

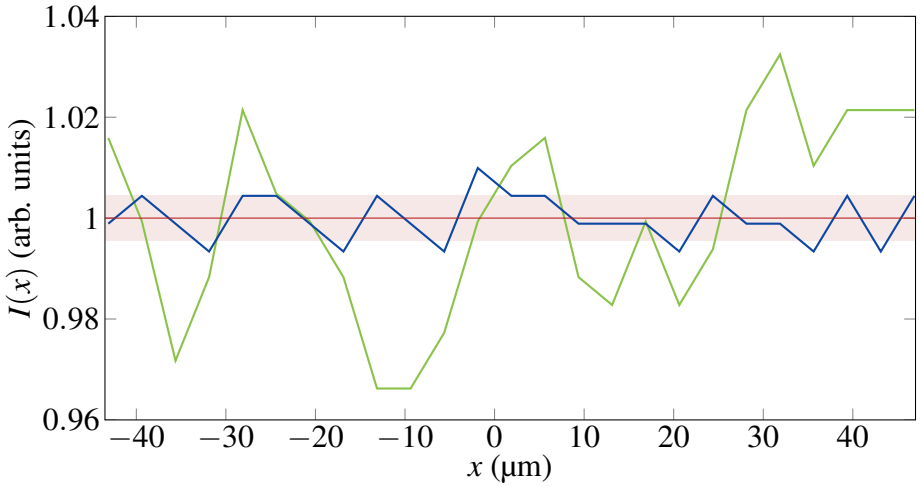

Fig. 6.7 Result of a manual pattern optimization with experimental feedback for the central region of a top-hat intensity profile after 61 steps. The AOI on the DMD chip has $n_x = 25$ and $n_y = 36$ pixels. The target intensity (red), initial intensity (green) and the final intensity profile (blue) are plotted for the region of interest on the CCD. The rms error of the initial and the final profile are $\varepsilon_{\text{rms}} = 1.7\%$ and $\varepsilon_{\text{rms}} = 0.46\%$ respectively. The interval shown in pink color indicates an averaged standard error of the measurement plotted in reference to the target due to the shot to shot fluctuations.

6.2 Pattern Optimization with Experimental Feedback

Simulating the imaging process might be useful to test optimization methods or even prepare an initial guess for the experiment, but it is incapable of including all details of the imaging system. So in order to achieve arbitrary 1d intensity profiles, the optimization has to be performed with feedback from experimental measurements.

Although the optimization method based on simulated annealing seems to be promising in numerical simulations, it turns out to be inefficient for optimizations with experimental feedback. In the simulations, the feedback is calculated within a few milliseconds, but in the experiment, a cycle takes up to 30 s (see 3.3), which means performing the same simulated annealing process presented in previous section would take more than a month time, during which the experiment will not be stable.

Having a pattern which produces a 1d intensity profile fairly close to the target might help to speed up the process. With such a pattern for an initial guess, running the simulated annealing process only at zero temperature (i.e only accepting steps lowering the energy) might lead to an optimized pattern. This decreases the optimization time dramatically from a month to a few hours. However, at zero temperature, there will be no means by which the

system can avoid local minima. This approach is discussed in the following with an example of pattern optimization with experimental feedback.

Here, the feedback process is performed using the intensity measured by a CCD camera. The 2d DMD pattern is imaged via the first demagnification stage (see 5.2) which allows for spatial filtering in x- and y-direction independently. The 1d intensity profile is obtained by averaging the intensity recorded by a single row of CCD pixels over multiple shots to suppress the error due to readout noise, photon shot-noise and laser intensity fluctuations.

In the example presented in figure 6.6, pattern optimization is performed for an AOI with $n_x = 100$ and $n_y = 150$ aiming to achieve a flat 1d top-hat intensity profile (red curve). The green curve in the figure presents the intensity profile produced by the initial pattern and the blue curve shows the intensity profile of the optimized pattern after 100 MC steps. In each step after flipping pixels randomly as explained in figure 6.1, averaging over 20 images provides the feedback.

In the region specified by the black rectangle, where the initial intensity is close to the target function, the optimization led to desired result as the error decreased from $\varepsilon_{\text{rms}} = 2.4\%$ to $\varepsilon_{\text{rms}} = 1.3\%$. Even the sharp edge to the right is smoothed out without performing additional spatial filtering in x-direction . On the other side, in the region marked with orange, the initial pattern did not produced an intensity close to target. As a consequence, the intensity did not optimized significantly within this 100 steps.

Although this optimization method is straightforward and feasible within a reasonable amount of time, it strongly depends on the initial state of the pattern and obtaining 1d intensity profiles with a desired precision is not guaranteed.

In order to confirm that the optimization process is not fundamentally limited by the physical properties of the system such as interferences, the central region of a top-hat intensity profile, similar to the previous example, is optimized manually. In this example, an AOI with $n_x = 25$ and $n_y = 36$ is optimized to obtain a smooth 1d intensity profile. As in the previous example, the feedback is provided by averaging over 20 images. In figure 6.7, green and blue curves represent the initial and the final intensity profiles respectively. The final intensity profile is clearly smoother than the initial profile as the rms error is decreased from $\varepsilon_{\text{rms}} = 1.7\%$ to $\varepsilon_{\text{rms}} = 0.46\%$. Further optimization was limited by the error produced by shot to shot fluctuations in the picture. This example shows that a deterministic optimization mechanism might work more efficiently than probabilistic ones.

An important point neglected in this chapter is the possibility of using the concept of time-averaging to gain extra levels of grayscales. As discussed in 4.4, based on the high pattern refresh rate of the DMD, this can allow for at least a factor of four increase in the number of grayscales in the experiment.

Finally, it is important to note that, even performing pattern optimization with experimental feedback provided by a CCD camera does not yield an ultimate 1d intensity profile which can be used in the experiment without further optimization. One reason is that the effects of the second demagnification stage can not be included in such optimizations. Another reason is that for the optimization with camera feedback, the camera itself will have an influence on the optimization process.

Chapter 7

Conclusion and Outlook

In the work presented in this thesis, an optical setup based on a digital micro mirror device (DMD) was designed, built and characterized. The system is capable of realizing both static and dynamic arbitrary 1d optical dipole potentials for neutral ^{87}Rb atoms in an cold atom experiment. A special focus of the thesis was to employ the concept of spatial filtering in a 4-f optical system to create arbitrary 1d intensity profiles with high grayscaling resolution, by imaging 2d binary DMD patterns. In the last chapter a probabilistic method was introduced to automatically design 2d DMD patterns leading to desired 1d intensity profiles.

During this work, all parts needed to install the system in the experimental setup were designed and built. After installation and alignment, the DMD setup will allow for realization of a whole zoo of trapping geometries enabling the investigation of a variety of interesting physics.

For example, flat bottom box-shaped potentials with different sizes can be realized. This potentials make the realization of homogeneous 1d density profiles possible which can be used to investigate recurrences in many-body quantum systems [36].

Through longitudinal splitting it will be possible to have more than one 1d systems along the 1d axis, which is not possible with the current trapping techniques in the experiment. Thermal machines can be realized through several box-shaped potentials with different depths, which can be dynamically coupled or decoupled, heated or cooled.

Analogue gravity models are another exciting topic that can be explored with 1d quasi-condensates. For example, Hawking radiation emitted from a sonic event horizon can be measured and characterized. Shaping the flow profile of the condensate through the underlying potential is a crucial ingredient in such experiments [13, 48, 49].

Furthermore, this setup will enable the realization of stable and reproducible random potentials necessary to study the interesting effects of disorder in cold atomic gases [50–52].

References

[1] A. Einstein, "Quantentheorie des einatomigen idealen Gases," *Sitzungsber. Kgl. Preuss. Akad. Wiss.*, p. 261, 1924.

[2] A. Einstein, "Quantentheorie des einatomigen idealen Gases (Zweite Abhandlung)," *Sitzungsber. Kgl. Preuss. Akad. Wiss.*, p. 3, 1925.

[3] S. Bose, "Plancks Gesetz und Lichtquantenhypothese," no. 26, p. 178, 1924.

[4] T. Maiman, "Ruby laser systems," Nov. 14 1967. US Patent 3,353,115.

[5] D. J. Wineland, R. E. Drullinger, and F. L. Walls, "Radiation-pressure cooling of bound resonant absorbers," *Phys. Rev. Lett.*, vol. 40, pp. 1639–1642, Jun 1978.

[6] W. D. Phillips and H. Metcalf, "Laser deceleration of an atomic beam," *Phys. Rev. Lett.*, vol. 48, pp. 596–599, Mar 1982.

[7] H. F. Hess, "Evaporative cooling of magnetically trapped and compressed spin-polarized hydrogen," *Phys. Rev. B*, vol. 34, pp. 3476–3479, Sep 1986.

[8] D. E. Pritchard, "Cooling neutral atoms in a magnetic trap for precision spectroscopy," *Phys. Rev. Lett.*, vol. 51, pp. 1336–1339, Oct 1983.

[9] A. L. Migdall, J. V. Prodan, W. D. Phillips, T. H. Bergeman, and H. J. Metcalf, "First observation of magnetically trapped neutral atoms," *Phys. Rev. Lett.*, vol. 54, pp. 2596–2599, Jun 1985.

[10] M. H. Anderson, J. R. Ensher, M. R. Matthews, C. E. Wieman, and E. A. Cornell, "Observation of bose-einstein condensation in a dilute atomic vapor," *Science*, vol. 269, no. 5221, pp. 198–201, 1995.

[11] K. B. Davis, M. O. Mewes, M. R. Andrews, N. J. van Druten, D. S. Durfee, D. M. Kurn, and W. Ketterle, "Bose-einstein condensation in a gas of sodium atoms," *Phys. Rev. Lett.*, vol. 75, pp. 3969–3973, Nov 1995.

[12] I. Bloch, J. Dalibard, and W. Zwerger, "Many-body physics with ultracold gases," *Rev. Mod. Phys.*, vol. 80, pp. 885–964, Jul 2008.

[13] J. Steinhauer, "Observation of quantum hawking radiation and its entanglement in an analogue black hole," *Nat Phys*, vol. 12, pp. 959–965, Oct 2016. Article.

[14] R. Folman, P. Krüger, D. Cassettari, B. Hessmo, T. Maier, and J. Schmiedmayer, "Controlling cold atoms using nanofabricated surfaces: Atom chips," *Phys. Rev. Lett.*, vol. 84, pp. 4749–4752, May 2000.

[15] R. Grimm, M. Weidemüller, and Y. B. Ovchinnikov, "Optical dipole traps for neutral atoms," vol. 42 of *Advances In Atomic, Molecular, and Optical Physics*, pp. 95 – 170, Academic Press, 2000.

[16] L. Hornbeck, "Spatial light modulator and method," Oct. 29 1991. US Patent 5,061,049.

[17] P. Krüger, X. Luo, M. W. Klein, K. Brugger, A. Haase, S. Wildermuth, S. Groth, I. Bar-Joseph, R. Folman, and J. Schmiedmayer, "Trapping and manipulating neutral atoms with electrostatic fields," *Phys. Rev. Lett.*, vol. 91, p. 233201, Dec 2003.

[18] S. Hofferberth, I. Lesanovsky, B. Fischer, J. Verdu, and J. Schmiedmayer, "Radiofrequency-dressed-state potentials for neutral atoms," *Nat Phys*, vol. 2, pp. 710–716, Oct 2006.

[19] J. Reichel, *Trapping and Manipulating Atoms on Chips*, pp. 33–60. Wiley-VCH Verlag GmbH & Co. KGaA, 2011.

[20] W. Hänsel, *Magnetische Mikrofallen für Rubidiumatome*. PhD thesis, Ludwig-Maximilians-Universität München, Fakultät für Physik, 2000.

[21] Y. V. Gott, M. S. Ioffe, and V. G. Tel'kovskii *Nucl. Fusion Suppl.*, vol. 3, p. 1045, 1962.

[22] K. Moore, T. Purdy, K. Murch, K. Brown, K. Dani, S. Gupta, and D. Stamper-Kurn, "Bose–einstein condensation in a mm-scale ioffe–pritchard trap," *Applied Physics B*, vol. 82, no. 4, pp. 533–538, 2006.

[23] R. Folman, P. Treutlein, and J. Schmiedmayer, *Atom Chip Fabrication*, pp. 61–117. Wiley-VCH Verlag GmbH & Co. KGaA, 2011.

[24] M. H. T. Extavour, L. J. LeBlanc, J. McKeever, A. B. Bardon, S. Aubin, S. Myrskog, T. Schumm, and J. H. Thywissen, *Fermions on Atom Chips*, pp. 365–394. Wiley-VCH Verlag GmbH & Co. KGaA, 2011.

[25] J. D. Carter, O. Cherry, and J. D. D. Martin, "Electric-field sensing near the surface microstructure of an atom chip using cold rydberg atoms," *Phys. Rev. A*, vol. 86, p. 053401, Nov 2012.

[26] S. A. Meek, H. Conrad, and G. Meijer, "Trapping molecules on a chip," *Science*, vol. 324, no. 5935, pp. 1699–1702, 2009.

[27] J. M. Amini, J. Britton, D. Leibfried, and D. J. Wineland, *Micro-Fabricated Chip Traps for Ions*, pp. 395–420. Wiley-VCH Verlag GmbH & Co. KGaA, 2011.

[28] A. Al-Rjoub and J. Verdú, "Electronic detection of a single particle in a coplanar-waveguide penning trap," *Applied Physics B*, vol. 107, no. 4, pp. 955–964, 2012.

[29] C. vom Hagen, *Towards a low-dimensional degenerate Fermi-Fermi-Bose mixture*. PhD thesis, Ruperto-Carola University of Heidelberg, Combined Faculties for the Natural Sciences and for Mathematics, 2008.

[30] M. Göbel, *Low-Dimensional Traps for Bose-Fermi Mixtures*. PhD thesis, Ruperto-Carola University of Heidelberg, Combined Faculties for the Natural Sciences and for Mathematics, 2008.

[31] M. Gring, *Prethermalization in an Isolated Many Body System*. PhD thesis, Technical University of Vienna, Faculty of Physics, 2012.

[32] I. Bouchoule, N. J. van Druten, and C. I. Westbrook, *Atom Chips and One-Dimensional Bose Gases*, pp. 331–363. Wiley-VCH Verlag GmbH & Co. KGaA, 2011.

[33] M. Brajdic, "Entwicklung einer Computersteuerung und ihre Anwendung in einem Experiment zur vereinfachten Bose-Einstein Kondensation in einer Oberflächenfalle," Master's thesis, Ruperto-Carola University of Heidelberg, Combined Faculties for the Natural Sciences and for Mathematics, 2003.

[34] W. Rohringer, "Stochastic optimization in an ultracold atom experiment," Master's thesis, Technical University of Vienna, Faculty of Physics, 2008.

[35] P. Krüger, L. M. Andersson, S. Wildermuth, S. Hofferberth, E. Haller, S. Aigner, S. Groth, I. Bar-Joseph, and J. Schmiedmayer, "Potential roughness near lithographically fabricated atom chips," *Phys. Rev. A*, vol. 76, p. 063621, Dec 2007.

[36] R. Geiger, T. Langen, I. E. Mazets, and J. Schmiedmayer, "Local relaxation and light-cone-like propagation of correlations in a trapped one-dimensional bose gas," *New Journal of Physics*, vol. 16, no. 5, p. 053034, 2014.

[37] T. Langen, R. Geiger, M. Kuhnert, B. Rauer, and J. Schmiedmayer, "Local emergence of thermal correlations in an isolated quantum many-body system," *Nat Phys*, vol. 9, pp. 640–643, Oct 2013. Letter.

[38] Texas Instruments, "Using lasers with DLP DMD technology," Sep 2008.

[39] H. Tamura, T. Unakami, J. He, Y. Miyamoto, and K. Nakagawa, "Highly uniform holographic microtrap arrays for single atom trapping using a feedback optimization of in-trap fluorescence measurements," *Opt. Express*, vol. 24, pp. 8132–8141, Apr 2016.

[40] P. Zupancic, P. M. Preiss, R. Ma, A. Lukin, M. E. Tai, M. Rispoli, R. Islam, and M. Greiner, "Ultra-precise holographic beam shaping for microscopic quantum control," *Opt. Express*, vol. 24, pp. 13881–13893, Jun 2016.

[41] L. D. Landau and E. M. Lifshitz, *Motion in rapidly oscillating field*, vol. 1 of *Courses of theoretical physics*, pp. 93–95. Butterworth-Heinemann, 1976.

[42] B. E. A. Saleh and M. C. Teich, *Fourier Optics*, pp. 108–156. John Wiley & Sons, Inc., 2001.

[43] B. E. A. Saleh and M. C. Teich, *Appendix B: Linear Systems*, pp. 928–933. John Wiley & Sons, Inc., 2001.

[44] B. E. A. Saleh and M. C. Teich, *Appendix A: Fourier Transform*, pp. 918–927. John Wiley & Sons, Inc., 2001.

[45] B. Stix, "A new imaging system for dual-species atomchip experiments," Master's thesis, Technical University of Vienna, Faculty of Physics, 2008.

[46] S. Kirkpatrick, C. D. Gelatt, and M. P. Vecchi, "Optimization by simulated annealing," *Science*, vol. 220, no. 4598, pp. 671–680, 1983.

[47] N. Metropolis, A. W. Rosenbluth, M. N. Rosenbluth, A. H. Teller, and E. Teller, "Equation of state calculations by fast computing machines," *The Journal of Chemical Physics*, vol. 21, no. 6, pp. 1087–1092, 1953.

[48] W. G. Unruh, "Experimental black-hole evaporation?," *Phys. Rev. Lett.*, vol. 46, pp. 1351–1353, May 1981.

[49] J. Steinhauer, "Observation of self-amplifying hawking radiation in an analogue black-hole laser," *Nat Phys*, vol. 10, pp. 864–869, Nov 2014. Article.

[50] G. Roati, C. D'Errico, L. Fallani, M. Fattori, C. Fort, M. Zaccanti, G. Modugno, M. Modugno, and M. Inguscio, "Anderson localization of a non-interacting bose-einstein condensate," *Nature*, vol. 453, pp. 895–898, Jun 2008.

[51] J. Billy, V. Josse, Z. Zuo, A. Bernard, B. Hambrecht, P. Lugan, D. Clement, L. Sanchez-Palencia, P. Bouyer, and A. Aspect, "Direct observation of anderson localization of matter waves in a controlled disorder," *Nature*, vol. 453, pp. 891–894, Jun 2008.

[52] M. Schreiber, S. S. Hodgman, P. Bordia, H. P. Lüschen, M. H. Fischer, R. Vosk, E. Altman, U. Schneider, and I. Bloch, "Observation of many-body localization of interacting fermions in a quasirandom optical lattice," *Science*, vol. 349, no. 6250, pp. 842–845, 2015.